Journal of Geophysical Research: Oceans

RESEARCH ARTICLE
10.1029/2018JC013965

The Density-Driven Winter Intensification of the Ross Sea Circulation

Stefan Jendersie[1,2], **Michael J. M. Williams**[1], **Pat J. Langhorne**[2], **and Robin Robertson**[3,4]

[1]National Institute of Water and Atmospheric Research, Wellington, New Zealand, [2]Department of Physics, University of Otago, Dunedin, New Zealand, [3]China-ASEAN College of Marine Science, Xiamen University Malaysia, Sepang, Selangor, Malaysia, [4]School of Physical, Environmental, and Mathematical Sciences, UNSW Canberra (ADFA), ACT, Australia

Key Points:
- Circulation in the Ross Sea intensifies throughout the course of winter
- Currents are predominantly density-driven and modulated by sea ice growth; wind stress dissipates lateral density gradients through mixing
- Circulation in the Ross Ice Shelf cavity is anticyclonic with inflow beside Ross Island; winds reduce melting by slowing the circulation

Correspondence to:
S. Jendersie,
stefan.jendersie@niwa.co.nz

Citation:
Jendersie, S., Williams, M., Langhorne, P. J., & Robertson, R. (2018). The density-driven winter intensification of the Ross Sea circulation. *Journal of Geophysical Research: Oceans*, *123*, 7702–7724. https://doi.org/10.1029/2018JC013965

Received 7 MAR 2018
Accepted 25 SEP 2018
Accepted article online 2 OCT 2018
Published online 5 NOV 2018

Abstract The circulation over the Ross Sea continental shelf facilitates the exchange between the Southern Ocean and the Ross Ice Shelf cavity. Here transport and mixing processes control the access of oceanic heat from the Southern Ocean to the ice shelf base, the formation of sea ice, and the production of High Salinity Shelf Water (HSSW) in polynyas and hence the subsequent formation of Antarctic Bottom Water. A climatological ocean-ice shelf coupled model of the Ross Sea Sector including the cavity, with prescribed sea ice fluxes, was used to examine the details of currents and their seasonal variability over the continental shelf. A system of two cyclonic and three anticyclonic persistent circulation features has been identified. Transports steadily increase throughout winter, with individual currents carrying up to 2 Sv, nearly doubling their minimum. The seasonal modulation is driven by lateral differences in density and subsequent baroclinic pressure gradients, induced through dense shelf water formation in the Ross Sea and the Terra Nova Bay Polynas. Wind plays a minor role in ocean momentum variability. Sensitivity experiments suggest a weakening of transports with increasing wind stress. Horizontal density variations at the ocean surface are smoothed by the wind. The source of momentum in the cavity is the gravity-driven bottom flow of HSSW, produced in the Ross Sea Polynya as part of the thermohaline overturning circulation. Tracer experiments suggest that HSSW forming in the Terra Nova Bay Polynya has no cavity access, but instead is the main contributor to Antarctic Bottom Water formed in the northwest slope.

Plain Language Summary The cavity beneath an ice shelf (Antarctica's massive floating glaciers) contains some of the most remote and poorly sampled waters on Earth. Yet these waters control the melting and stability of ice shelves and their ability to prevent the accelerated discharge of Antarctica's grounded ice sheets into the ocean. Such catastrophic events would cause global sea level rise. Here computer simulations are used to link together sparse observations and understand the present-day behavior of the ocean beneath the Ross Ice Shelf, the largest ice shelf on Earth. We focus on the seasonal patterns and drivers of ocean currents in the Ross Sea which transport heat from deep in the Southern Ocean to the Ross Ice Shelf. The simulations show that currents are driven by horizontal differences in density induced by rapid winter sea ice formation on a wind-swept, partially open, ocean. Yet in regions of more complete sea ice cover stronger winds reduce the circulation by mixing water masses of different density and smoothing out density differences. Slower currents would carry less heat into the Ross Ice Shelf cavity, reducing melting there. Establishing the circulation's indirect wind dependency adds an important detail in predicting the future of the Ross Ice Shelf.

1. Introduction

Antarctic ice shelves play a key role in protecting the grounded Antarctic ice sheets, by buttressing against increased ice sheet discharge (Dupont, 2005; Joughin & Alley, 2011). Accelerated mass loss as a result of ice shelf disintegration has already been observed on the West Antarctic Peninsula (WAP; Joughin et al., 2012; Rignot et al., 2004), so much so that a collapse of the West Antarctic Ice Sheet is regarded as a possible future scenario (Joughin & Alley, 2011; Thomas et al., 2004). The fate of the Ross Ice Shelf (RIS) is crucial to the stability of the West Antarctic Ice Sheet which is largely grounded below sea level (Joughin & Alley, 2011).

The shielding of the grounding line from warm ocean water is difficult to observe. Grounding line melting from oceanic heat causes the transition zone between the floating shelf and grounded sheet to retreat (Walker et al., 2008). It is estimated that more than half of the mass loss of Antarctic ice shelves is driven by the ocean

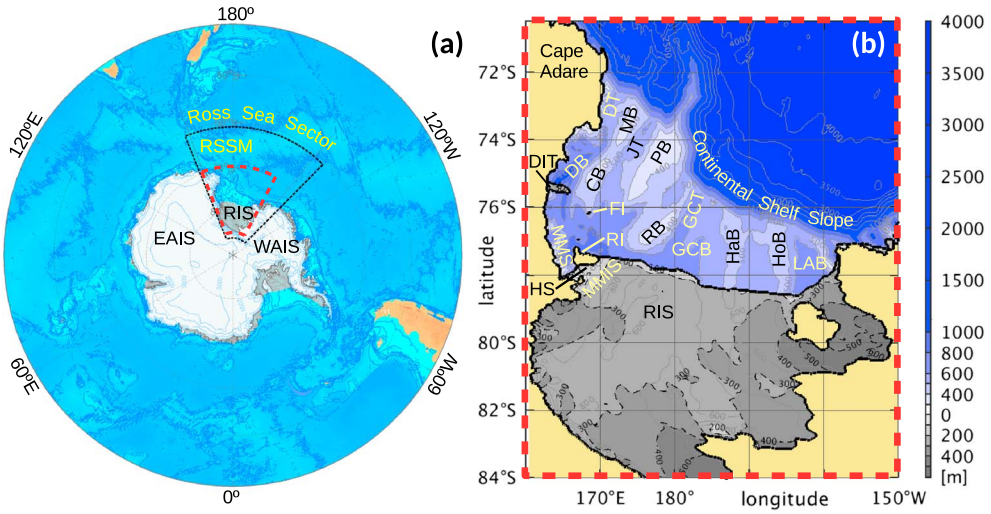

Figure 1. (a) Thin black dashed lines mark the RSSM domain bounds. (b) The region of focus, the Ross Sea continental shelf with topographical features. The cropped region corresponds to the red dashed line in (a). The color scale is blue for ocean depth and gray for ice shelf draft. Topographical features are: (a) RIS = Ross Ice Shelf; WAIS = West Antarctic Ice Sheet; EAIS = East Antarctic Ice Sheet; (b) DT = Drygalski Trough; DB = Drygalski Basin; DIT = Drygalski Ice Tongue; RI = Ross Island; FI = Franklin Island; MMS = McMurdo Sound; MMIS = McMurdo Ice Shelf; MB = Mawson Bank; CB = Crary Bank; JT = Joides Trough; PB = Pennell Bank; RB = Ross Bank; GCB = Glomar Challenger Basin; GCT = Glomar Challenger Trough; HaB = Hayes Bank; HoB = Houtz Bank; HS = Haskell Strait; LAB = Little America Basin. RSSM = Ross Sea Sector Model.

(total basal melt: 1516 ± 106 Gt per year; RIS: 27 ± 22 Gt per year; total calving flux: 755 ± 25 Gt per year; Liu et al., 2015). Consequently, changes in ocean state inevitably affect the stability of Antarctica's ice sheets. Observation and model studies have investigated the already evident changes in the Southern Ocean and those predicted as consequences of future climate change. An intensification and southward shift of winds over the Antarctic Circumpolar Current toward the Antarctic continent has been measured over five decades (Marshall, 2003). Observations also show a strengthening of the northward, cold katabatic winds over the RIS (Turner et al., 2009), possibly increasing the sea ice production (Comiso et al., 2011). Counter intuitively a freshening of maximum High Salinity Shelf Water (HSSW) salinities in the Ross Sea by 0.03 per decade has been observed in the past six decades (Jacobs et al., 2002; Jacobs & Giulivi, 2010), highlighting the complexity and nonlinearity of feedback mechanisms.

The two main water masses responsible for basal ice shelf melting are HSSW, mostly formed in the polynyas, and relatively warm Circumpolar Deep Water (CDW) shoaling to shallower depths within the Antarctic Slope Current (ASC). The types of melting caused by the two water masses are commonly termed ice shelf melting modes 1 and 2 (Jacobs et al., 1992, 2011; MacAyeal, 1984; Orsi & Wiederwohl, 2009; Petty et al., 2014; I. J. Smith et al., 2012; W. O. Smith et al., 2012). The future production of HSSW is inevitably linked to changes in sea ice formation intensity and volume. CDW intruding onto the shelf mixes with surface and shelf waters to form modified CDW (mCDW; Dinniman et al., 2011; Jacobs, 1991; Kohut et al., 2013). Results from numerical model studies show that CDW has gained increased access to the continental shelves in the Amundsen Sea and along the WAP (Dinniman et al., 2012; Thoma et al., 2008). For the Ross Sea, simulations predict a general decrease in on-shelf advection of CDW (Smith et al., 2014) for 2050 and 2100 climate scenarios. For the Filchner-Ronne Ice Shelf, Timmermann and Hellmer (2013) suggest that a 4–6 times higher basal mass loss by the 22nd century (present 90 Gt per year) will be driven by increased access of CDW to the deep ice shelf grounding line.

Understanding the advection of these water masses toward the RIS, which is separated from the shelf break by several hundred kilometers of shallower continental shelf (mean depth of ~530 m), is a crucial aspect in assessing the future RIS stability in the advent of a warming climate. Although some circulation features of the Ross Sea continental shelf are known (Ashford et al., 2012; Carter et al., 2008; Dinniman et al., 2011; W. O. Smith et al., 2012; Smith et al., 2014), understanding the seasonal variability is hampered due to the lack of winter-time data. Under the interior of the RIS, few oceanographic measurements exist to date (Jacobs et al., 1979), hence the specific patterns of ocean currents in the cavity can only be inferred from numerical models. It has

long been established that the ocean dynamics under ice shelves are largely decoupled from the momentum in the ocean outside, with the main source of momentum being buoyancy (Jenkins, 1991; MacAyeal, 1984).

In this study we use a numerical, climatologically forced Regional Ocean Modeling System (ROMS) ocean circulation model encompassing the Ross Sea Sector to establish the main flow patterns over the continental shelf, including within the RIS cavity (Figures 1a and 1b). We determine the transports, seasonal variability, and sensitivity to tides and wind forcing of the flow patterns. In particular, we investigate the individual flow pathways of HSSW formed in the Ross Sea Polynya (RSP) and the Terra Nova Bay Polynya (TNBP) and the location of mCDW over the continental shelf. In combination with passive tracer experiments, further analysis focusses on the access of these water masses to the ocean cavity under the RIS.

2. Methods: The Ross Sea Sector Model

This study uses a version of the ROMS 3.4 (Rutgers; Shchepetkin & McWilliams, 2005; with adaptation from Galton-Fenzi et al., 2012), a free-surface, primitive equation, terrain-following stretched-coordinate ocean circulation model. It is coupled to a thermodynamic ice shelf module (Robertson et al., 2003) to simulate melting and refreezing at the base of ice shelves with constant ice draft. The model domain incorporates the RIS ocean cavity and the smaller Sulzburger, Nickerson, and part of the Getz Ice Shelf cavities which are to the east of the RIS. The horizontal grid resolution ranges from 9.8 to 2.7 km along the northern and southern model boundaries at 61°S and 85°, respectively (4.6 km at the eastern shelf break, defined as the 800 m isobath; 3.8 km near the ice shelf edge). The 24 vertical sigma-layers are concentrated toward the bottom and the surface in order to better resolve vertical mixing processes near the ice shelf base and gravity-driven bottom flows (Jenkins, 1991). The gridded bathymetry interpolated from the RTopo-1 and Davey maps (Davey, 2004; Timmermann et al., 2010) was smoothed where changes in the water column height (bathymetry and ice shelf draft) are large with respect to the total depth. Mixing of active tracers is along geopotential surfaces, and momentum along sigma-levels. Momentum advection is third-order upstream bias for 3-D momentum and fourth-order centered for 2-D momentum using a Smagorinsky-like viscosity. Vertical mixing uses the Mellor-Yamada 2.5 mixing algorithm (Allen et al., 1995; Galperin et al., 1988; Mellor & Yamada, 1982) that maintains a separate explicit prognostic formulation of turbulent kinetic energy. ROMS tidal forcing utilized the modified version from Robertson (2006) to simulate the constituents M2, S2, K1, and O1 with coefficients retrieved from TPXO7.1 (Egbert & Erofeeva, 2002).

Horizontal tracer advection is facilitated through a modified positive-definite recursive, third-order accurate MPDATA scheme (Margolin & Smolarkiewicz, 1998; Smolarkiewicz, 1984). From testing different available advection schemes in ROMS, MPDATA handled the relatively steep ice shelf front in our application. In its original description by Margolin and Smolarkiewicz (1998), the tracer coefficient in the antidiffusive calculation violates the $-1 \leq A \leq 1$ requirement only at velocity points between numerical grid boxes with tracer concentration of different presign. The subsequent high numerical diffusion is limited to the first order advection value and retains conservation. While this may be sufficient to simulate the continental shelf Ross Sea where temperatures are mostly negative, the ROMS implementation of MPDATA disables the corrective antidiffusive velocity for negative tracers entirely. In order to use MPDATA in the polar ocean environment, we modified it for temperature. Following Smolarkiewicz and Clark (1986), a constant of 10 is added to the tracer field before advection is computed and subsequently subtracted for other operations including calculation of density.

2.1. Boundary Conditions

Temperature and salinity at the lateral open boundaries are nudged to the World Ocean Atlas 2009 climatology (Antonov et al., 2010; Locarnini et al., 2010), biased toward property imports to the domain. Boundary values for depth-averaged transports were constructed from Global Ocean Data Assimilation System (Behringer & Xue, 2004) retrieved velocities. Applied as radiation conditions, they are combined with Chapman conditions for the free surface, ζ, to allow perturbations to radiate out. Sea ice is not explicitly simulated in the Ross Sea Sector Model (RSSM). Instead, surface boundary conditions are imposed heat and freshwater fluxes, as derived from Special Sensor Microwave Imager (SSM/I) observations (Tamura et al., 2008). This flux-prescribing method is similar to that applied in other modeling studies (Cougnon et al., 2013; Dinniman et al., 2011; Galton-Fenzi et al., 2012; Gwyther et al., 2014; Hattermann et al., 2014). The 12.5-km flux fields were interpolated onto the finer RSSM grid and subsequently smoothed applying a Gaussian Window mean of 7×7 grid cells (~25 km in the RSP). In the region of the RSP the data show inconsistencies with the RTopo-1-retrieved land and ice shelf masks and show the edge too far north. In order to maintain the

Table 1
Dissipation Functions Tested in the Sensitivity Experiments and Names of the Corresponding Simulation Cases

Wind stress dissipation	Simulation cases	
	With tides	No tides
$\mathcal{D}_A^\tau = 0$	A_t	A_{nt}
$\mathcal{D}_B^\tau = \left\{ \begin{array}{ll} 1 & \text{for } c^{si} < 0.5 \\ 2\left(1 - c^{si}\right) & \text{for } c^{si} \geq 0.5 \end{array} \right\}$	B_t	B_{nt}
$\mathcal{D}_C^\tau = 1 - e^{\left(10c^{si} - 10\right)}$	C_t	C_{nt}
$\mathcal{D}_D^\tau = 1$	D_t	D_{nt}

overall salt input and heat loss in winter, as prescribed by the data, the RSP signal extrema were not extrapolated toward the model RIS edge. Freshwater fluxes are entirely sourced from SSM/I. In contrast, summer surface heat fluxes are horizontally interpolated from 1.875° monthly averages of the NCEP-DOE 2 Reanalysis (Kanamitsu et al., 2002) and temporally blended with the SSM/I-derived fields by applying a simple ramp scheme. June–September are 100% SSM/I, and January–February are 100% NCEP-DOE with monthly ramping steps of 25% between these periods. All surface fluxes, wind stress forcing (NCEP/NCAR Reanalysis 1, Kalnay et al., 1996), and the boundary transports are monthly values, climatologically averaged over 1992–2007.

Initially, summer heat fluxes for the RSSM were derived from NCEP/NCAR Reanalysis 1, (Kalnay et al., 1996) which lead to unrealistically high surface temperatures. NCEP/NCAR heat flux data are known to largely overestimate sensible and latent thermal exchange by up to 51%, in particular for high wind speeds and large ocean-air temperature gradients. The misrepresentation was due to inconsistent heat and moisture roughness length formulations in the turbulent heat exchange algorithm (Renfrew et al., 2002). The newer bulk algorithm in NCEP-DOE computes more realistic heat fluxes for the polar and subpolar regions that are used in this study. While potentially desirable to have also used the NCEP-DOE wind fields, there is no evidence that the NCEP/NCAR wind fields have significant issues (Kanamitsu et al., 2002). They are frequently used in other studies to either force models or supplement observations (Abernathey et al., 2016; Comiso et al., 2011; Hollands et al., 2013; Kusahara et al., 2011; Nøst et al., 2011; Reddy et al., 2010). Hence, we decided to maintain consistency with our earlier work by retaining the NCEP/NCAR wind fields.

The exchange between water and the ice shelf base is governed by the three equation formulation (Hellmer & Olbers, 1989; Holland & Jenkins, 1999), with modification from Jenkins et al. (2001), Robertson et al. (2003), and Robertson (2013). Jenkins et al. (2001) provide an explicit formulation of melt water advection without changes in the kinematic boundary conditions, maintaining conservation and preventing solution drift in long-term model integrations. Robertson et al. (2003) and Robertson (2013) increase mixing in the boundary layer by assuming velocity profiles to be of common log instead of natural log shape. Their second adjustment accounts for nonzero melting at vanishing velocities by assuming that diffusion fluxes maintain a minimum salinity of 5 at the interface. Both modifications serve to circumnavigate the asymptotic behavior of the turbulent transfer coefficient in slow circulation environments like large parts of the south-eastern RIS cavity. An alternative method not used here but with similar effects as described in Gwyther et al. (2016) maintains a minimum friction velocity threshold.

2.2. Wind Stress Sensitivity Experiment

An abundance of studies exists on the thermodynamic exchange between ocean, sea ice, and atmosphere and on sea ice drift due to winds and ocean currents. Many have investigated the role of sea ice in atmosphere-induced upper ocean turbulence and mixing (Cole et al., 2014; Feltham, 2002; Fer et al., 2004; Fer & Sundfjord, 2007; Goosse & Fichefet, 1999; Lenn et al., 2011; McPhee, 2002, 1992; McPhee et al., 1987; McPhee & Martinson, 1994; Peterson et al., 2017; Petty et al., 2013; Robertson et al., 1995; Skyllingstad & Denbo, 2001; Stevens et al., 2009).

There are fewer investigations explicitly on the role of sea ice in the ocean momentum response to atmospheric stress, that is, Ekman Transport (Mensa & Timmermans, 2017; Nøst et al., 2011). The challenge is to quantify the energy transfer coefficient from atmosphere to ocean when sea ice internal stresses act to balance some of the stress applied by winds. The drag force imparted on the atmosphere is no longer equal to

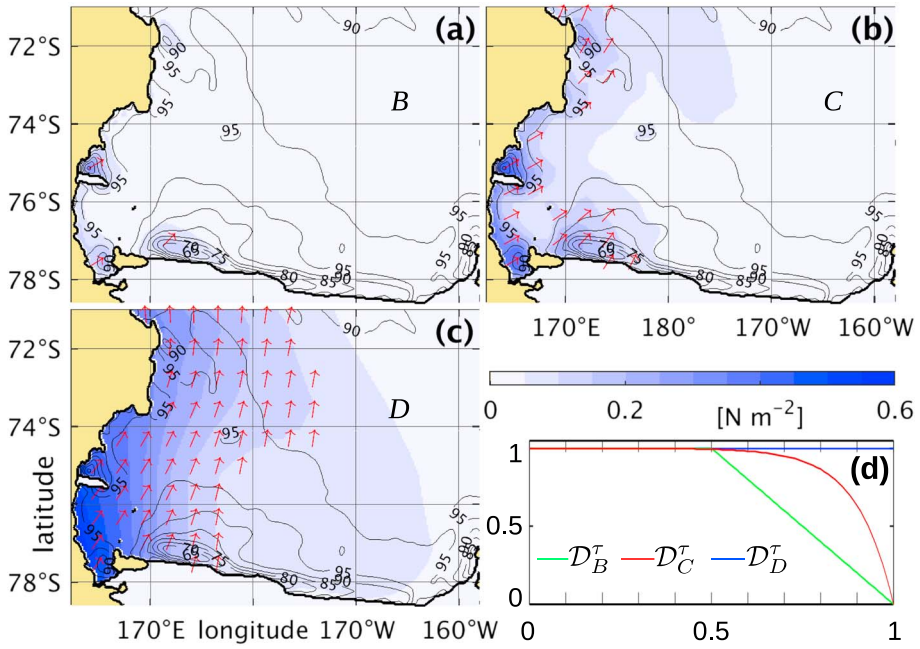

Figure 2. (a)–(c) Wind stress τ, model boundary field in August for the simulation cases of the sensitivity study. Background color is the wind stress magnitude, red arrows show the wind stress direction for τ>0.1 N m^{-2}, black contours are sea ice concentration in [%]. (d) Corresponding wind stress dissipation coefficients $\mathcal{D}^{\tau}$ as a function of the sea ice concentration c^{si} in units of fraction. Note that wind stress for cases *B*, *C*, and *D* are approximately the same in regions of persistent polynya activity. Not shown are boundary field and dissipation function for *A* with $\mathcal{D}^{\tau}_{A} = 0$, $\boldsymbol{\tau} = 0$, that is, zero wind stress over the entire domain.

the force acting on the ocean surface. Lüpkes and Birnbaum (2005) found that the drag coefficient, hence stress, applied to the atmosphere increases with increasing sea ice concentrations up to 60%. We assume that this effect is included in observation-supported wind stress data sets. Nøst et al. (2011) suggest that, at 80% sea ice concentration, the average drag coefficient applied to the ocean surface drops to half of that proposed by Lüpkes and Birnbaum (2005) for the atmosphere, that is, a step function shaped dissipation function describing the translation of atmospheric stress to ocean stress with sea ice. Drift speeds of sea ice floes are of the order of 1.5–2% of the driving wind (McPhee, 1980, 2002, 2008). Therefore, we hypothesize that sea ice cover close to 100% should largely shield the ocean from atmospheric momentum, that is, the dissipation coefficient, as introduced later in this section, should be close to zero. Furthermore, wind-driven ice floes in sufficiently unimpeded drift deviate by ~25° to the left (southern hemisphere) from the surface wind stress direction (Leppäranta, 2011; McPhee, 1980). This adds a rotation component to the stress imparted on the ocean.

To investigate the effects of sea ice on surface stress deviation and dissipation, and the subsequent ocean circulation response, four simulations were performed with different wind stress formulations applied as boundary forcings: a zero wind stress over the whole domain and three modified stress vector fields. For the nonzero cases surface stress boundaries were retrieved from the NCEP/NCAR Reanalysis 1 data set (Kalnay et al., 1996). After constructing climatological monthly averages over 1992–2007 ($\boldsymbol{\tau}_{NCEP}$), fields were subjected to three versions of the sea ice dependent dissipation and deviation algorithm

$$\boldsymbol{\tau} = \mathcal{R}^{\tau}(c^{si})D^{\tau}(c^{si})\boldsymbol{\tau}_{NCEP}.$$

$c^{si} = \{0 \dots 1\}$ is the sea ice concentration (ASI algorithm, SSMI-SSMIS) retrieved as 5-day median filtered, gap-filled product for 1992–2007 from ICDC (http://icdc.cen.uni-hamburg.de; Kaleschke et al., 2001; Kern et al., 2010; Spreen et al., 2008). The deviation is

$$\mathcal{R}^{\tau} = \begin{pmatrix} \cos(\alpha) & \sin(\alpha) \\ -\sin(\alpha) & \cos(\alpha) \end{pmatrix}, \quad \text{with} \quad \alpha = -25°c^{si} + 0°(1 - c^{si}),$$

the mean drift deviation angle, computed as a linear combination of ice covered and open ocean surface.

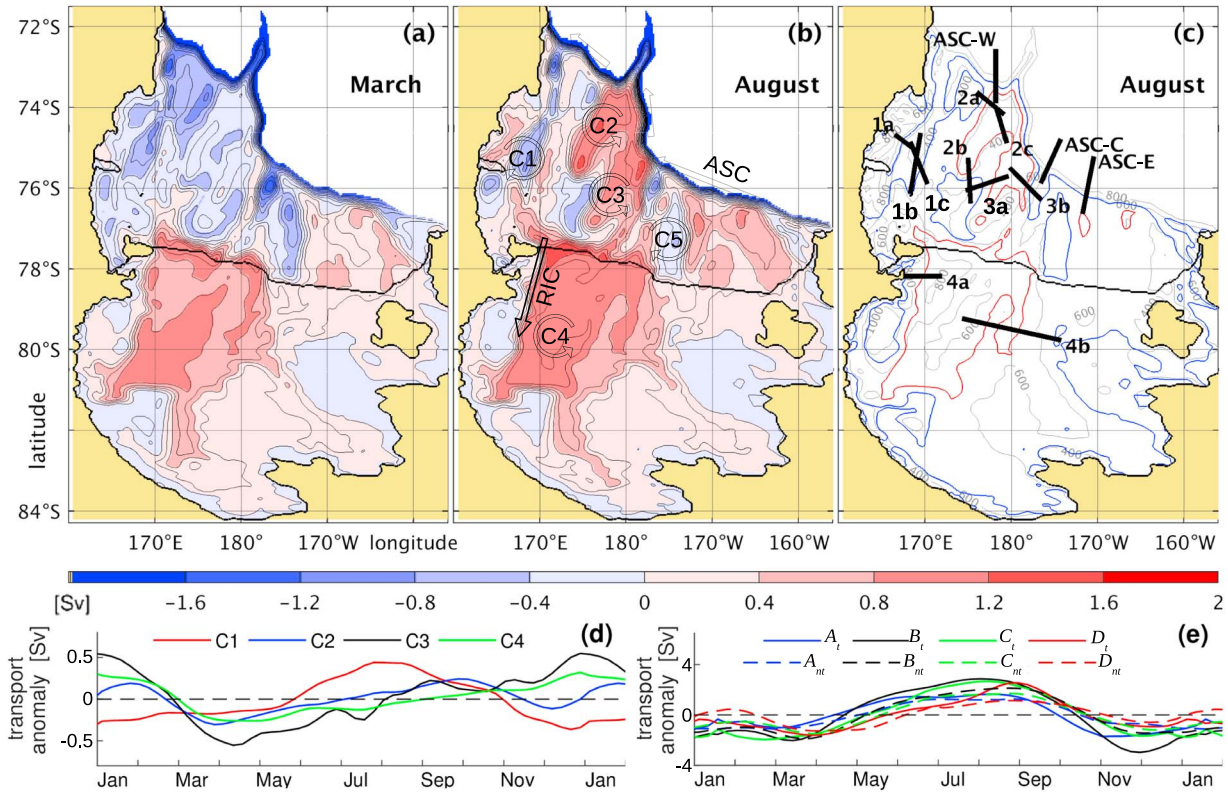

Figure 3. Ross Sea circulation patterns and transport anomalies. (a)and (b) Depth integrated stream function ψ showing the circulation pattern over the continental shelf in March and August. Minima are cyclonic (clockwise, blue) circulation features, maxima indicate anticyclonic structures (red). Features are labeled as ASC = Antarctic Slope Current, RIC = Ross Island Current. (c) Color contours are a replot of two stream function levels for August to mark the bounds of the cyclonic (blue, 0 Sv) and anticyclonic (red, 0.8 Sv) circulation features as labeled in (b). Gray contours are bathymetry. (d) Intra-annual transport anomaly of the circulation features as labeled in (c) for the most realistic C_t case. Circulation transports are calculated as the average of transports across individual transects: C1 across 1a, 1b, 1c; C2 across 2a, 2b, 2c; C3 across 3a, 3b; and C4 across 4a, 4b as labeled in (c). The annual means of C1–4 are 0.9, 1.0, 1.4, and 1.1 Sv, respectively. (e) Intra-annual transport anomaly of the ASC in eight simulations across the four wind stress schemes, with (full lines) and without tides (dashed). Values in all panels correspond to an average over 4 simulated years after 8 years spin-up.

The stress dissipation functions $\mathcal{D}^\tau$ tested in this study are listed in Table 1, along with the corresponding simulation cases for tidal and nontidal versions. For sea ice cover of 0–50%, $\mathcal{D}^\tau_B$ and $\mathcal{D}^\tau_C$ are equivalent to $\mathcal{D}^\tau_D$, applying the full strength of τ_{NCEP} as surface forcing (Figure 2d). For concentrations greater than 50%, $\mathcal{D}^\tau_B$ tests a linear response of ocean surface stress to sea ice cover, while $\mathcal{D}^\tau_C$ explores an exponential response that limits the shielding effect to high sea ice concentrations. These two functions envelope the 0.5 stress dissipation coefficient at 80% sea ice cover as proposed by Nøst et al. (2011), but may provide a more realistic dissipation dependency than Nøst et al. (2011). $\mathcal{D}^\tau_B$ and $\mathcal{D}^\tau_C$ also adhere to the hypothesis of zero ocean stress at 100% sea ice cover. The resulting stress fields for August are shown in Figure 2.

The transfer mediation of atmospheric stress to the ocean in Mensa and Timmermans (2017) is realized by use of a sea ice model (Zhang & Hibler, 1997). Unfortunately, no parameterization of the stress dissipation is given for use in studies without a sea ice model, neither are we aware of available constraints from observation. Therefore, assuming the effect exists, the realistic simulation with lesser stress dissipation by sea ice, C_t, was chosen as the control case. It served to perform the circulation and water mass transport analysis in section 3.

2.3. Tracer Experiments

Different water masses (CDW and mCDW, HSSW and melt water) were tracked using a total of six nondissipative, online passive tracers, starting after an 8-year model spin-up. Inflowing water below depths of 300 m with potential density anomaly of 27.78 kg/m^3 $< \sigma <$ 27.82 kg/m^3 and potential temperature θ>1° C at the eastern model domain boundary was assigned with an initial CDW concentration of 1. In order to distinguish between HSSW formed in the RSP and in the TNBP, at each site a separate tracer was placed in the model's

Table 2
Results of the Sensitivity Study Across Four Different Wind Stress Schemes, With and Without Tides

Simulation cases	A_t	B_t	**C_t**	D_t	A_{nt}	B_{nt}	C_{nt}	D_{nt}
Wind stress [N/m^2]								
Slope region, northwest	0	0.04	**0.08**	0.14	0	0.04	0.08	0.14
Drygalski Basin/Trough	0	0.05	**0.10**	0.19	0	0.05	0.10	0.19
Ross Sea cont. shelf	0	0.04	**0.08**	0.13	0	0.04	0.08	0.13
RSP	0	0.13	**0.08**	0.16	0	0.13	0.16	0.16
Transports [Sv]								
Ross I. Current, sw (C4)	1.25	1.25	**1.11**	0.91	1.28	1.23	1.13	0.89
Central cavity, nw (C4)	0.98	1.01	**1.03**	0.79	1.04	0.99	1	0.76
Joides Trough, sw (C2)	1.11	0.77	**0.82**	0.32	1.06	1.01	1.00	0.29
Drygalski, nw (C1)	1.19	0.90	**0.70**	0.58	1.17	0.83	0.65	0.61
Ross Bank, nw (C3,C5)	2.31	2.13	**2.05**	1.61	2.29	2.10	2.03	1.63
ASC-E, ww	3.32	11.15	**13.52**	12.28	3.41	4.09	4.82	6.33
ASC-C, ww	2.84	9.52	**11.73**	10.84	2.79	3.33	3.84	5.00
ASC-W, ww	7.42	11.71	**12.46**	11.32	7.34	7.07	7.38	6.91
HSSW [Sv]								
McMurdo, sw	0.27	0.33	**0.36**	0.31	0.23	0.24	0.28	0.43
Past 79°S, sw (C4)	1.27	1.21	**0.91**	0.41	1.29	1.23	1.14	0.96
Glomar Ch., nw (C3,C5)	0.60	0.50	**0.40**	0.14	1.09	0.9	0.66	0.34
Drygaslki, nw (C1)	0.46	0.48	**0.54**	0.44	0.48	0.57	0.71	0.94
mCDW southward [Sv]								
Total, 100 km on-shelf	2.10	1.47	**1.29**	1.29	1.94	1.75	1.40	1.19
Drygalski, (C1)	0.79	0.43	**0.26**	0.24	0.72	0.47	0.26	0.21
Pennell Bank, (C2)	0.86	0.69	**0.66**	0.43	0.80	0.83	0.69	0.36
Hayes Bank, (C5)	96	11	**7**	6	63	30	17	22 [mSv]
Hayes B., under RIS	1	1	**1**	0	2	2	3	4 [mSv]
Heat southward [TW]								
Total, 100 km on-shelf	9.84	8.28	**6.85**	6.2	9.69	8.58	7.12	6.33
Past 79°S	0.46	0.27	**0.24**	0.17	0.35	0.28	0.25	0.18
Temperature [°C]								
Cavity average	−1.87	−1.95	**−1.96**	−1.97	−1.89	−1.95	−1.96	−1.96
Melt rate [cm/year]								
Melting	14.7	10.8	**9.7**	7.9	14.5	11.1	9.7	8.0
Refreezing	1.2	0.8	**0.7**	0.6	1.2	0.9	0.8	0.6

Note. Case C_t serves as the base for results in section 3, all cases are evaluated, compared, and discussed in section 4. Water mass transports are given in [Sv], except mCDW along Hayes Bank is in [mSV]; nw = northward flows; sw = southward; ww = westward. Note that the Drygalski Trough facilitates a bidirectional flow system. Southward flowing mCDW sits on top of northbound HSSW which dominates the volume flux budget, making C1 cyclonic. RSP = Ross Sea Polynya; ASC = Antarctic Slope Current; HSSW = High Salinity Shelf Water; CB = Crary Bank; mCDW = modified Circumpolar Deep Water; RIS = Ross Ice Shelf.

surface grid cells when $S > 34.70$ and $\theta < -1.85°$ C at times of sea ice production. HSSW tracer units were chosen to be proportional to the model's surface salt flux to account for the different polynya intensities. Melt water from the ice shelf base was tracked using a similar method. Three formation sites were discriminated with separate tracers for McMurdo Ice Shelf (MMIS) with ice draft shallower than 250 m and west of 177.33°E; the RIS front, ice draft shallower than 250 m, east of 177.33°E; and the grounding line. Tracers with units proportional to the ice shelf-ocean fresh water flux are placed at times of melting. All tracers are passively advected and diffused using the same coefficients for vertical mixing and horizontal diffusion as for the RSSM's temperature and salinity.

3. Results and Discussion: Circulation and Water Masses in the C_t Case

All simulations in this study are initialized in mid-January and run climatologically forced for 12 years, encompassing 8 years of spin-up. Results presented here are weekly means averaged over the last 4 years of model integration. Model time references of passive tracer figures are individually marked.

3.1. The Main Circulation Features

Transport in the ASC (assessed across transect ASC-W, Figure 3c) exhibits a strong seasonal variability, with lows, smaller than 11 Sv from December through February and maximum transports in July–August that exceed 15 Sv (Table 2, Figure 3e). The width and the zonal position of the ASC are seasonally changing (±10 km, not shown). This path variation is not temporally homogeneous along the shelf break. It has been suggested by Gordon et al. (2009) and Padman et al. (2009) that it is linked with the off-shelf export of dense HSSW in this region.

The monthly mean circulation in the Ross Sea for March and August is illustrated by the stream function ψ in Figures 3a and 3b. The ψ for each horizontal model grid cell is calculated from the simulated west to east depth-averaged velocities $\bar{U}$, the ocean water column thickness h, sea surface height ζ, and the corresponding cell's metric width Δs as

$$\psi_{i+\frac{1}{2},j+\frac{1}{2}} = \psi_{i+\frac{1}{2},j-\frac{1}{2}} + \bar{U}_{i+\frac{1}{2},j}\left(h_{i+\frac{1}{2},j} + \zeta_{i+\frac{1}{2},j}\right)\Delta s_{i+\frac{1}{2},j}.$$

The i and j are the west-east and south-north running model grid cell indices. Transport budgets in Figures 3d and 3e and Table 2 were obtained by tracking and filtering the largest individual flowband within a transect. Values represent the net flow within one flowband, not the entire transect.

Three large anticyclonic circulation features were identified, ventilating the western central shelf and the ocean cavity. The centers are located over Pennell Bank (C2 in Figure 3b; Figure 1b for topographical names), Ross Bank (C3), and under the western half of the RIS (C4). The zonal flows along the north-south running troughs agree with schematic views of currents over the shelf in Ashford et al. (2012) and Smith et al. (2014), which are based on the ROMS model of Dinniman et al. (2007) with resolutions comparable to the RSSM. Mean transports of C2, C3, and C4 are 1.0, 1.4, and 1.1 Sv, respectively. Two cyclonic features: C1, associated with Crary Bank, 0.9 Sv, and C5 (Glomar Challenger Basin, 0.5 Sv) facilitate the water exchange over the northwestern and the central-eastern shelf.

Generally, the circulation intensifies in winter although the seasonal evolution is different for individual features (Figure 3d). The anomaly range is up to 1.0 Sv in the open ocean and 0.6 Sv inside the cavity (range is calculated as difference between seasonal maximum and minimum). The beginning of April, when the circulation is weakest, marks the start of flow intensification in the open ocean. Individual peak transports are reached in August, September, and December–January (C1, C2, and C3, respectively). C2 experiences a second transport maximum in January. The circulation in the cavity (C4) is weakest during March to May and intensifies continuously until December. The main inflow of water underneath the RIS, hereafter named *Ross Island Current*, is via the 800 m deep and ~100 km wide channel east of Ross Island (Figures 3a and 3b).

3.2. Access Gateways for mCDW

The passive tracer experiment identified Drygalski Trough (C1), Joides Trough (C2), and the western slope of Hayes Bank (C5) as the main intrusion pathways for CDW/mCDW onto the Ross Sea continental shelf (Figure 4a). This is consistent with other modeling and observation-based studies (Dinniman et al., 2011; Jacobs, 1991; Klinck & Dinniman, 2010; Kohut et al., 2013; Orsi & Wiederwohl, 2009).

The RSSM oceanographic outputs yield an average net volume of 1.3 Sv of mCDW (bounds of 27.75 kg/m^3 $< \sigma <$ 27.85 kg/m^3, $\theta > -1.5$° C) advected into the interior of the continental shelf, between ~100 km south of the shelf break and the RIS front (transect 3 in Figures 4a and 4c; Table 2). This sits within the estimates from other simulation studies (0.37 Sv, Dinniman et al., 2003; 2.10 ± 0.54 Sv, Smith et al., 2014), which vary due to different methods employed.

The driving mechanism of the ASC and in particular the processes by which CDW is diverted across the shelf break was not investigated in this study. Assessing bathymetry-guided mesoscale eddies, one of the three responsible mechanisms (Stewart & Thompson, 2015; St-Laurent et al., 2013), requires a numerical grid spacing of at least a factor 2 less than the baroclinic deformation radius $r=c/f$ (Coriolis parameter f, wave speed c; Hallberg, 2013; Klinck & Dinniman, 2010). A horizontal resolution of ~2 km at the Ross Sea continental shelf break would be required to incorporate these processes into the analysis.

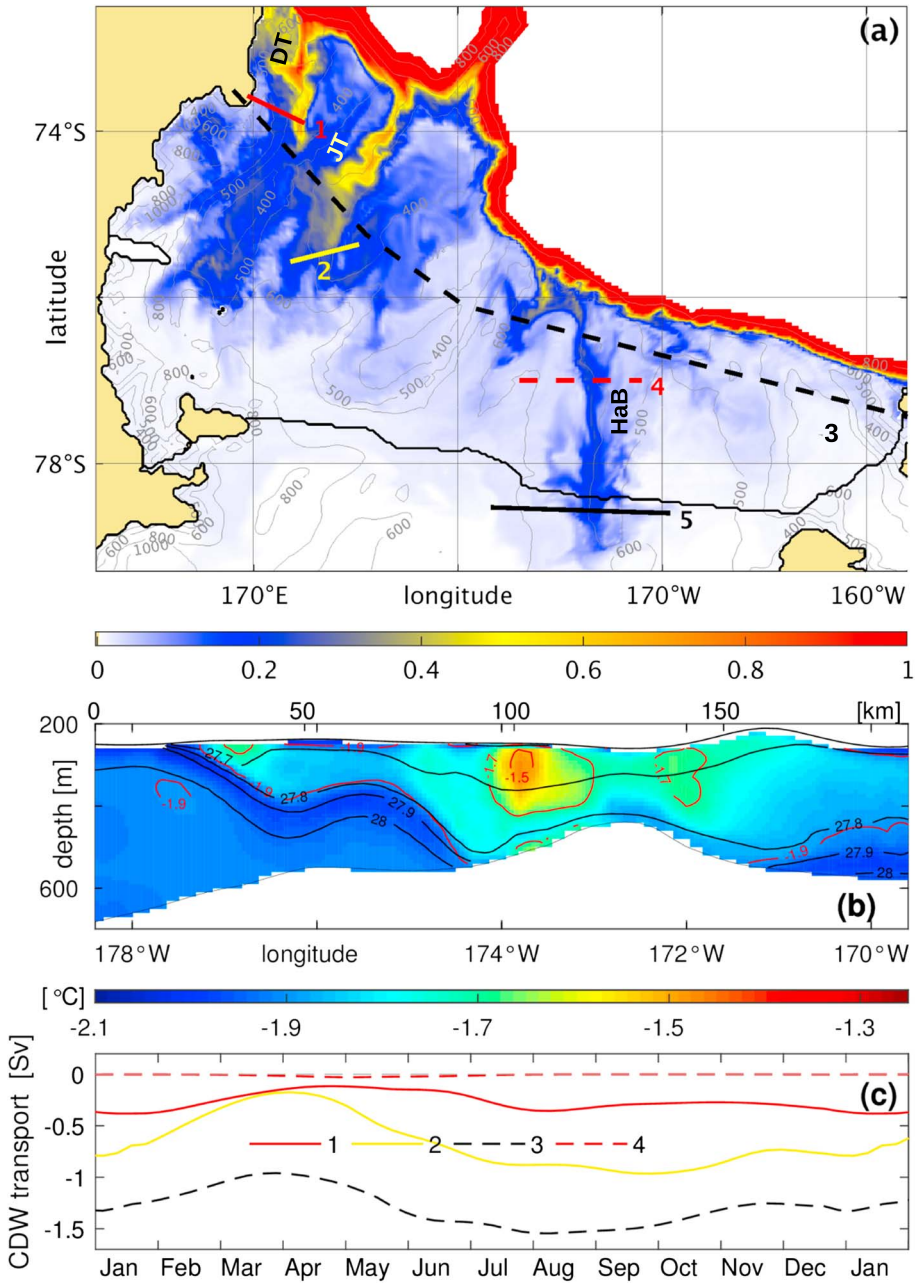

Figure 4. CDW/mCDW intrusion over the continental shelf. (a) Top view of maximum over depth of mCDW tracer value on the continental shelf. Color units are dye tracer concentration, normalized to the off-shelf value, where CDW is expected to be pure (red, concentration of 1). (b) Northward view of transect 5 in (a) showing the mCDW intrusion under the Ross Ice Shelf in May, within 20 km of the ice front. Color unit is potential temperature. Contours: black is density anomaly [kg/m^3]; red is potential temperature [° C]. (c) Intrusion volumes of CDW/mCDW from analyzing oceanographic properties (not tracer concentration). All values are negative southward, the transect locations are shown in the corresponding line style in (a). DT = Drygalski Trough; JT = Joides Trough; HaB = Hayes Bank; CDW = Circumpolar Deep Water; mCDW = modified CDW.

3.2.1. Drygalski Trough and Drygalski Basin

In January–February, and in August, the slope between Drygalski Trough and Mawson Bank guides bursts of up to 0.4 Sv mCDW southward (transect 1 in Figures 4a and 4c, Table 2). The twofold seasonality and timing of on-flow along Drygalski Trough is confirmed by in situ observation in Castagno et al. (2016), although the temporal pattern in the model appears about 1 month later than observed. The inflow minimum in April–May

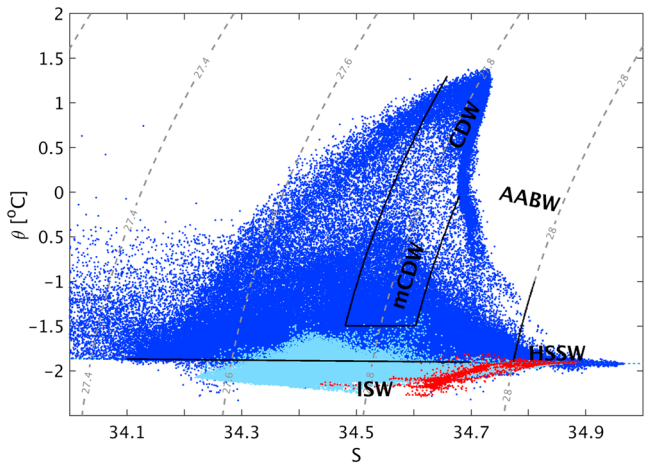

Figure 5. Potential temperature and salinity scatter plot for Ross Sea Sector Model water mass representation for three separate ocean regions. **Blue** is all the continental shelf, including the slope shallower than 1,500 m, and the cavity immediately beyond the ice shelf front, north of 78°S. **Light blue** shows mixing between mCDW, HSSW, and melt water in the frontal cavity region over Hayes Bank. **Red** is mixing between HSSW and melt water near the grounding line. The water mass bounds used for transport assessments in this study are marked as CDW and mCDW with potential density anomaly 27.75 kg/m^3 $< \sigma <$ 27.85 kg/m^3, and potential temperature $\theta > -1.5°$ C; HSSW, $\sigma >$ 28 kg/m^3; ISW, $\theta < -1.92°$ C. AABW = Antarctic Bottom Water; CDW = Circumpolar Deep Water; mCDW = modified CDW; HSSW = High Salinity Shelf Water; ISW = Ice Shelf Water.

coincides with comparably strong, northward recirculation events (0.1 Sv). Thus, Drygalski Trough accounts for an average net southward flow of 0.2 Sv of mCDW.

The CDW tracer experiment results suggest that mCDW intruding south along Drygalski Trough swaps from Mawson Bank's western slope to the eastern slope of Crary Bank, thus entering the clockwise circulation of C1. Toward Franklin Island the current turns northwest and deposits mCDW into the Drygalski Basin. Possible observational evidence for mCDW in Terra Nova Bay can be found in Stevens et al. (2017; their Figure 7, inset showing the full data set of CTD profiles around the Drygalski Ice Tongue).

RSSM outputs indicate that a seasonal strengthening and on-shelf movement of the ASC enables flows to attach to isobaths with access to the continental shelf (not shown). First suggested by Klinck and Dinniman (2010), this hypothesis has recently found observational support in Castagno et al. (2016) and may explain the seasonal variability of southward mCDW transport in Drygalski Trough.

3.2.2. Joides Trough

Circulation feature C2, via Joides Trough, carries an average of 0.7 Sv of mCDW to the southern extent of Pennell Bank (transect 2 in Figures 4a and 4c; Table 2) which is more than twice that of observation-based estimates of 0.24 Sv in early February (Kohut et al., 2013). The RSSM suggests peak on-shelf flows close to 1 Sv from July through October and a seasonal minimum of less than 0.2 Sv in April.

Small traces of mCDW flowing south via Joides Trough appear to be deposited in the depression between Ross Island, Ross Bank, and Franklin Island (less than 10% of the off-shelf CDW tracer concentration). Although our tracer study suggests that from here mCDW eventually enters the cavity via the Ross Island Current as part of C4, we argue that the heat signature would be eliminated by the RSP deep convection at the beginning of winter.

3.2.3. Glomar Challenger Basin

C5, situated in the Glomar Challenger Basin, is the only current that links CDW/mCDW from the shelf break directly to the RIS (Figure 4a). While greater volumes of mCDW enter and circulate within the northern Glomar Challenger Basin, a comparably low average of 7 mSv are advected further south along the western slope of Hayes Bank and deposited before the ice shelf front (transect 4 in Figures 4a and 4c). In the model, between 10% and 50% of this deposit eventually penetrates south into the RIS cavity. It stays bathymetrically confined to Hayes Bank, and shows no significant seasonal variability (transect 5 in Figures 4a and 4b; not shown in 4c). The ridge, and subsequently the mCDW signal, terminates at ~79°S (Figure 4a). Under the ice shelf, half of the mCDW is transformed (light blue in Figure 5) with the remaining quantities being recirculated northward, out of the cavity.

The existence of a warm water core over Hayes Bank has been measured during various RIS front transects (Jacobs & Giulivi, 1999; Jacobs & Weiss, 1998). Its intrusion southward past the RIS front was suggested by a number of model studies (Dinniman et al., 2011; Holland et al., 2003; Reddy et al., 2010).Recirculation events were detected in moorings along the RIS front (Bergamasco et al., 2002), but the southernmost extent of mCDW into the cavity has not been observed.

3.3. HSSW—Formation and Pathways

The RSSM's polynyas produce an average of 0.85 Sv of HSSW ($\sigma >$ 28 kg/m^3, Figure 5), of which 33% (0.28 Sv) forms in the TNBP. Although the total is lower than the estimated limit of >1 Sv given by (Gordon et al., 2009), it should be noted that their estimate includes only 0.2 Sv of directly observed HSSW outflow from the AnSlope and CLIMA experiments in the Drygalski Basin/Trough region. The remaining budget was inferred from 0.86 Sv of ISW production estimates by Smethie and Jacobs (2005) who based their melt rate calculation (19.0 cm/year) on observed differences between in and outflowing water properties near the RIS front. However, Smethie and Jacobs (2005) emphasized the difficulty in inferring melt rates and ISW production volumes from salinity budgets. A similar calculation based on changes in HSSW temperature yielded melt rate estimates of 6.7 cm/year, smaller by 65% (Smethie & Jacobs, 2005). Applying the same assumption as

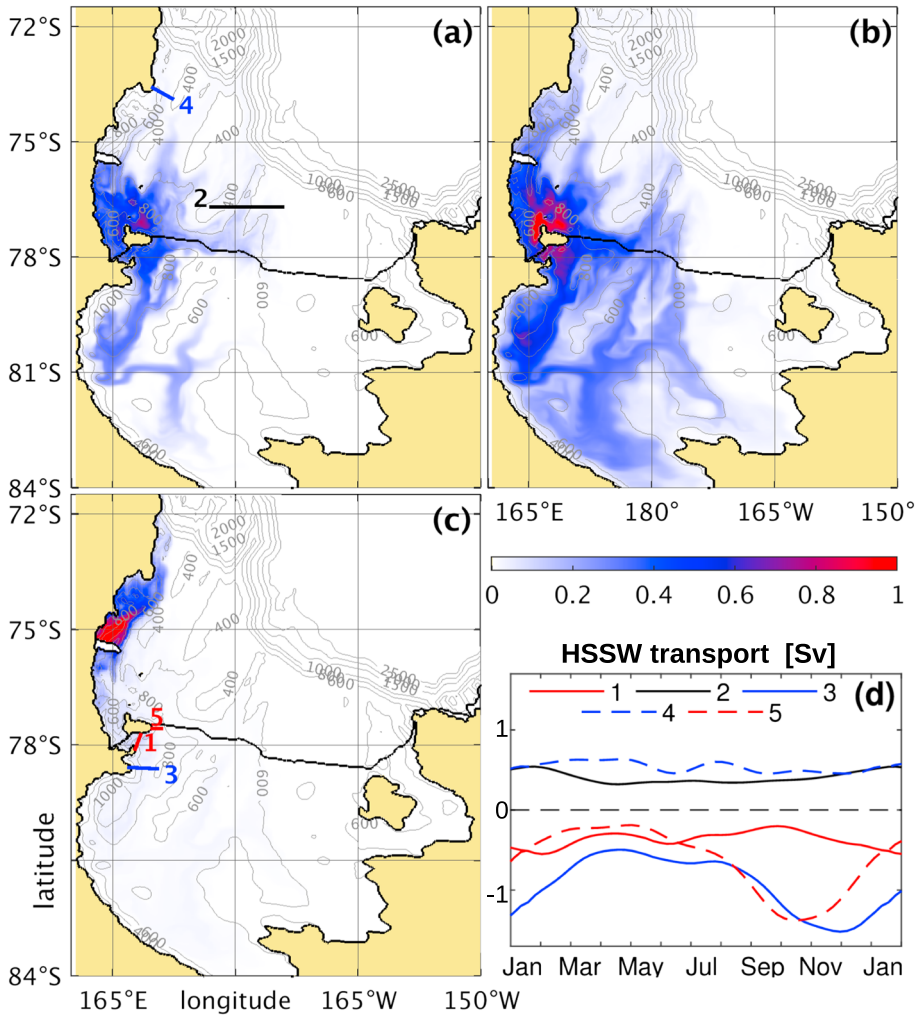

Figure 6. HSSW presence in the Ross Sea, derived from the nondissipative passive tracer experiments. Color values are proportional to the depth integrated salt mass induced by sea ice production, scaled and normalized to one. (a) HSSW tracer budget produced in the RSP over one season at the end of the following summer (February, simulation year 2); (b) three seasons of HSSW tracer in the RSP at the end of summer (February, year 4). (c) Three seasons of Terra Nova Bay Polynya HSSW production (February, year 4). Time periods for (a) and (b) were chosen to illustrate both the pathways and the residence areas of RSP HSSW. (d) HSSW transports obtained by the Ross Sea Sector Model's oceanographic outputs. Transects 1, 3, and 5 are southward through Haskell Strait, past 79°S, and via the Ross Island Current, respectively; Transects 2 and 4 are northward along Glomar Challenger Trough and Drygalski Trough. Transects are marked in (a) and (c). HSSW = High Salinity Shelf Water; RSP = Ross Sea Polynya.

Gordon et al. (2009), our analysis would yield 1.4 Sv HSSW production. Furthermore, their HSSW definition is slightly less restrictive than the one used here (respectively, S>34.70 compared to S > ~34.77, equivalent to $\sigma > 28$ kg/m^3 at surface freezing temperature). This was chosen to represent the densest water produced in the model and to capture kinetic effects caused by differences in density like geostrophic currents and gravity-driven currents.

In the RSSM, a separation of HSSW from the TNBP and RSP formation sites is evident (Figures 6a–6c). Only comparably small quantities of TNBP HSSW protrude further south than the southern extent of the Drygalski Basin 800 m isobath at 76.4°S. Instead 0.54 Sv of HSSW flows toward the shelf break (transect 4 in Figure 6d, transect locations shown in Figures 6a and 6c) which is consistent with estimates in other studies which found 0.2–0.5 Sv for HSSW exports through the Drygalski Trough (Gordon et al., 2009; Q. Wang et al., 2010).The RSSM's export in this location is twice as big as the initial HSSW production in the TNBP. Two processes contribute. First, the HSSW volume (as discriminated by the $\sigma > 28.0$ kg/m^3 threshold) is increased by mixing

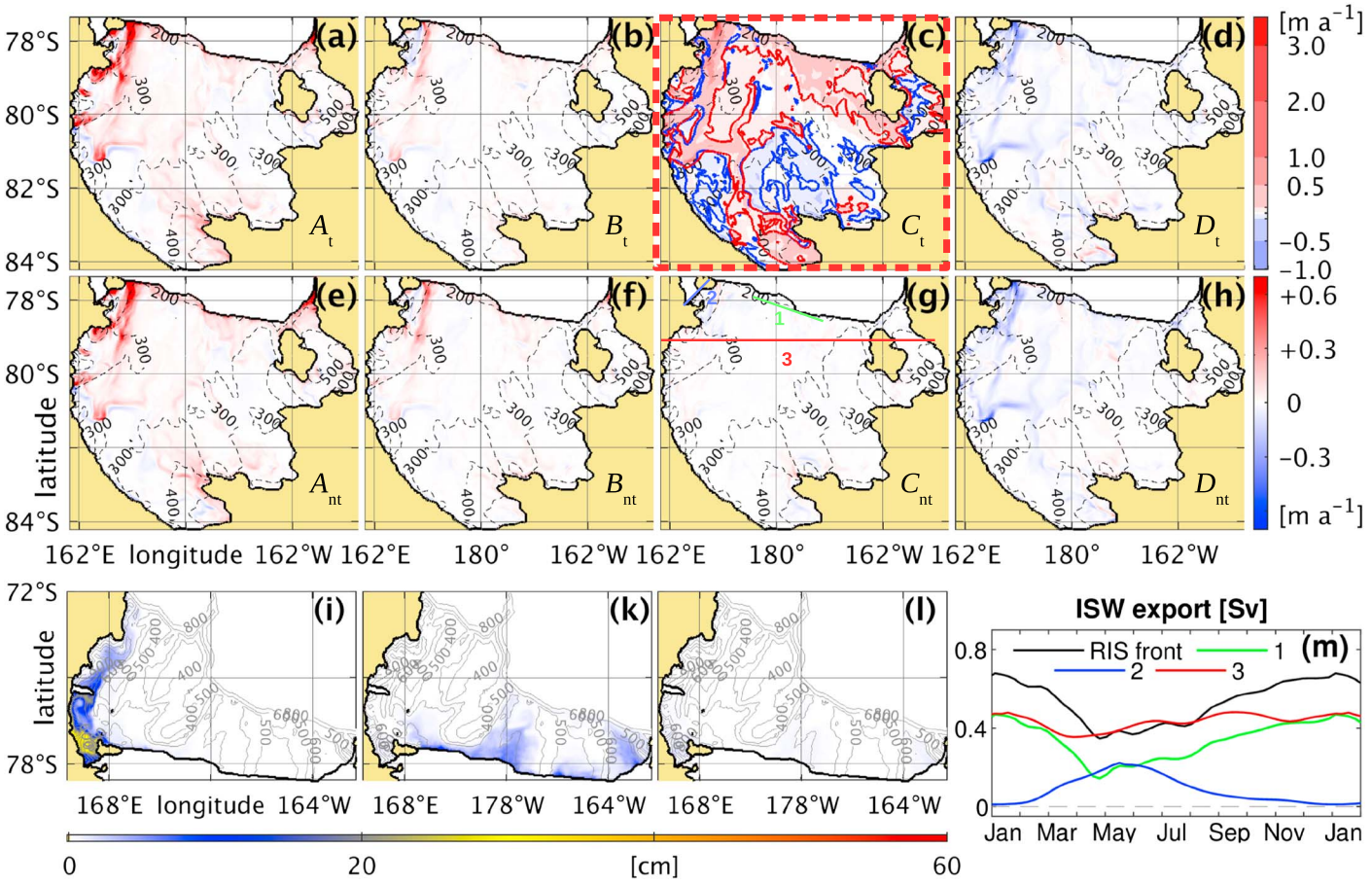

Figure 7. Annual refreezing and melting at the base of the RIS, ISW pathways, and transports. (c) Shows melting and refreezing patterns of the C_t case. The color scale (top right colorbar) is blue for refreezing, red is for melting. White is the open ocean and any area that experiences a net melt or freeze rate of less than 0.01 m/year. Gray dashed contours are ice shelf draft. The thick blue and red contours enclose regions that show maximum seasonal refreezing of more than 0.01 m/year and maximum seasonal melting greater than 1 m/year, respectively. (a), (b), and (d)–(h) show the difference to (c), that is, blue is less melting/more refreezing, red indicates more melting/less refreezing (bottom right colorbar). Melt tracer experiment. (i) Melt water originating from the McMurdo Ice Shelf; (k) from the RIS frontal region; (l) from the grounding line. The color unit is depth integrated water column height of pure melt water. ISW export budgets in (m), except the blue line are computed for water of $\theta < -1.92$°C. Black is net outflow from the entire RIS front, green is from the center of the RIS into Glomar Challenger Basin (transect 1 in (g)) and the red line shows the net ISW northward flow from the remote cavity (across 79°S, transect 3). The blue curve (transect 2 in (g)), showing ISW flux through Haskell Strait into McMurdo Sound, is computed for water fresher than 34.7 and colder than −1.5° C. RIS = Ross Ice Shelf; ISW = Ice Shelf Water.

of the dense water in Drygalski Basin with lighter shelf water, and possibly mCDW, residing in the dynamic circulation regime over the adjacent Crary Bank. The second contribution is from the RSP.

Most of the HSSW, produced in the RSP and the McMurdo Polynya, is advected under the RIS and the MMIS via the Ross Island Current and through the Haskell Strait. Unlike the suggestions of Mahoney et al. (2011), we find that the additional salt entering McMurdo Sound in winter is not sourced from the TNBP, but almost entirely from the RSP. 0.91 Sv of HSSW enters the remote RIS cavity, southward of 79°S (transect 3 in Figure 6d). Thus, the propelling of the circulation in C4 depends on gravity-driven, dense water bottom flows. Results from the RSSM suggest that more than 10% of the HSSW, advected to the southern part of the RIS (south of 79°S), is sufficiently mixed with ice shelf melt (red in Figure 5) to become lighter than 28 kg/m^3 (HSSW threshold in this study).

The main outflow gate of HSSW from the cavity is around 180° opening into the Glomar Challenger Basin where it merges with younger but smaller HSSW volumes imported directly from the RSP via C3 over Ross Bank (Figures 6a and 6b). Near the date line observations confirm the presence of a persistent 50–100 m thick HSSW bottom layer, although it is not clear whether this has transited the cavity or is directly sourced from the RSP (Jacobs & Giulivi, 1999; Smethie & Jacobs, 2005). In the RSSM, eventually 0.40 Sv of HSSW flows

toward the shelf break (Table 2, transect 2 in Figure 6d), along the slope between Ross Bank and Glomar Challenger Trough as part of the joint northward current of circulation features C3 and C5 (Figure 3b). This volume accounts for about half in the RSSM's total off-shelf export of 0.94 Sv Ross Sea HSSW (measured across transect 3 shown in Figure 4a).

While the total is greater than the observation-based estimate range 0.5–0.8 Sv, the simulated presence of HSSW along Drygalski Basin/Trough, Joides Trough, and Glomar Challenger Trough is well established by measurements (Gordon et al., 2004, 2009; Muench et al., 2009; Orsi & Wiederwohl, 2009).

3.4. Ice Shelf Melting and ISW export

The average net melt rate (melting minus refreezing) of 9.0 cm/year in the RSSM (C_t case in Table 2) is at the lower end of the range of estimates for RIS melt (8–60 cm/year) from other studies (Arzeno et al., 2014; Assmann et al., 2003; Assmann & Timmermann, 2005; Depoorter et al., 2013; Dinniman et al., 2007, 2011; Hellmer, 2004; Holland et al., 2003; Jacobs et al., 1979; 1992; Lazeroms et al., 2018; Liu et al., 2015; Moholdt et al., 2014; Reddy et al., 2010; Rignot et al., 2013; Smethie & Jacobs, 2005; Timmermann et al., 2012). Studies that use numerical simulations yield an average of 30 $\pm$ 19 cm/year, while the observation-based studies suggest 16 $\pm$ 6 cm/year. Nevertheless, the RSSM net melt rate agrees particularly well with more recent observation derived values of 10 $\pm$ 1 and 11 $\pm$ 14 cm/year (Liu et al., 2015; Moholdt et al., 2014).

Areas of high melt in the RSSM (enclosed red in Figure 7c) are concentrated along the HSSW inflow pathway in the west, the frontal region, at the grounding line, and the mCDW intrusion over Hayes Bank, near 170°W (compare mCDW intrusion in Figure 4a). Regions of net-freezing are evident in the central cavity. While the regional melt patterns in the tidal case largely agree with findings of Arzeno et al. (2014; using a ROMS model from Dinniman et al., 2007, 2011, with added tides and sea ice model), their melt rate of 32 cm/year is greater than this study.

The coupled sea ice model (Budgell, 2005) and added tides in Arzeno et al. (2014) are the main modification from Dinniman et al. (2011) who instead apply a surface flux prescription method, similar to the RSSM. The 15.3 cm/year net melt rate in Dinniman et al. (2011) is much closer to the RSSM's 8.9 cm/year (C_{nt}, Table 2) than to 25 cm/year nontidal value found by Arzeno et al. (2014). While Arzeno et al. (2014) estimate 35% of their modeled ice loss is generated in the immediate frontal zone of the RIS, this is unlikely to explain the melt rate differences. Due to the smoothing of water column thickness that is often required in sigma-coordinate models, the front of ice shelves may allow an unrealistic amount of Mode 3 melting, that is, access of surface-warmed water (Jacobs et al., 1992). For comparison, the Arzeno et al. (2014) model ice draft at their northern mooring location is 80 m, while the RSSM's 180 m is much closer to the actual 219 m. The use of a sea ice model and the shallower ice draft near the front, which is more accessible for surface heat, may thus explain the higher net melt rates in Arzeno et al. (2014).

ISW generated in the RSSM ($\theta < -1.92°$ C, Figure 5) is exported from the cavity at an annual average of 0.5 Sv with seasonal peaks reaching 0.7 Sv (black line in Figure 7m). This is less than available observation-based estimates of 1.4 and 0.86 Sv by Jacobs et al. (1992) and Smethie and Jacobs (2005). Comparing the black and red lines in Figure 7m suggests that ~20% of ISW under the RIS is generated north of 79°S. This region includes the MMIS, the cavity inflow path via the Ross Island Current, and the mCDW-affected region over Hayes Bank.

Results from the passive tracer experiment, shown in Figures 7i, 7k, and 7l, illustrate where melt water originating from (i) the MMIS, (k) the frontal region, and (l) from the grounding line exits the cavity. Consistent with oceanographic measurements the main outflow gates of ISW open into Glomar Challenger Basin and the western side of McMurdo Sound (Barry & Dayton, 1988; Bergamasco et al., 1999; Hughes et al., 2014; Lewis & Perkin, 1985; Orsi & Wiederwohl, 2009; Robinson et al., 2010, 2014; Tressler & Ommundsen, 1962).

In the Glomar Challenger Basin ISW outflows have a maximum in December (0.4 Sv, transect 1 in Figure 7m) and a minimum in April–May. The annual mean of 0.3 Sv is comparable to observation-based estimates of 0.15 and 0.28 Sv for 1995 and 1996, respectively (Bergamasco et al., 2002). The RSSM's temporal and spatial ISW export characteristics of pulsed outflows with recirculation events on the order of days to 1 week (not visible in the weekly averages used in Figure 7m) match the Bergamasco et al. (2002) mooring data in that location.

Along Haskell Strait the RSSM's melt water tracer strongly correlates with a freshening signature, in contrast to temperatures below surface freezing point at the other ISW outflow regions. Therefore, the ISW fluxes in this location (blue line in Figure 7m) were alternatively calculated for water with $S < 34.7$ and $\theta < -1.5°$ C, and are not included in the overall ISW budget. The model's ISW outflow through McMurdo Sound is greater than

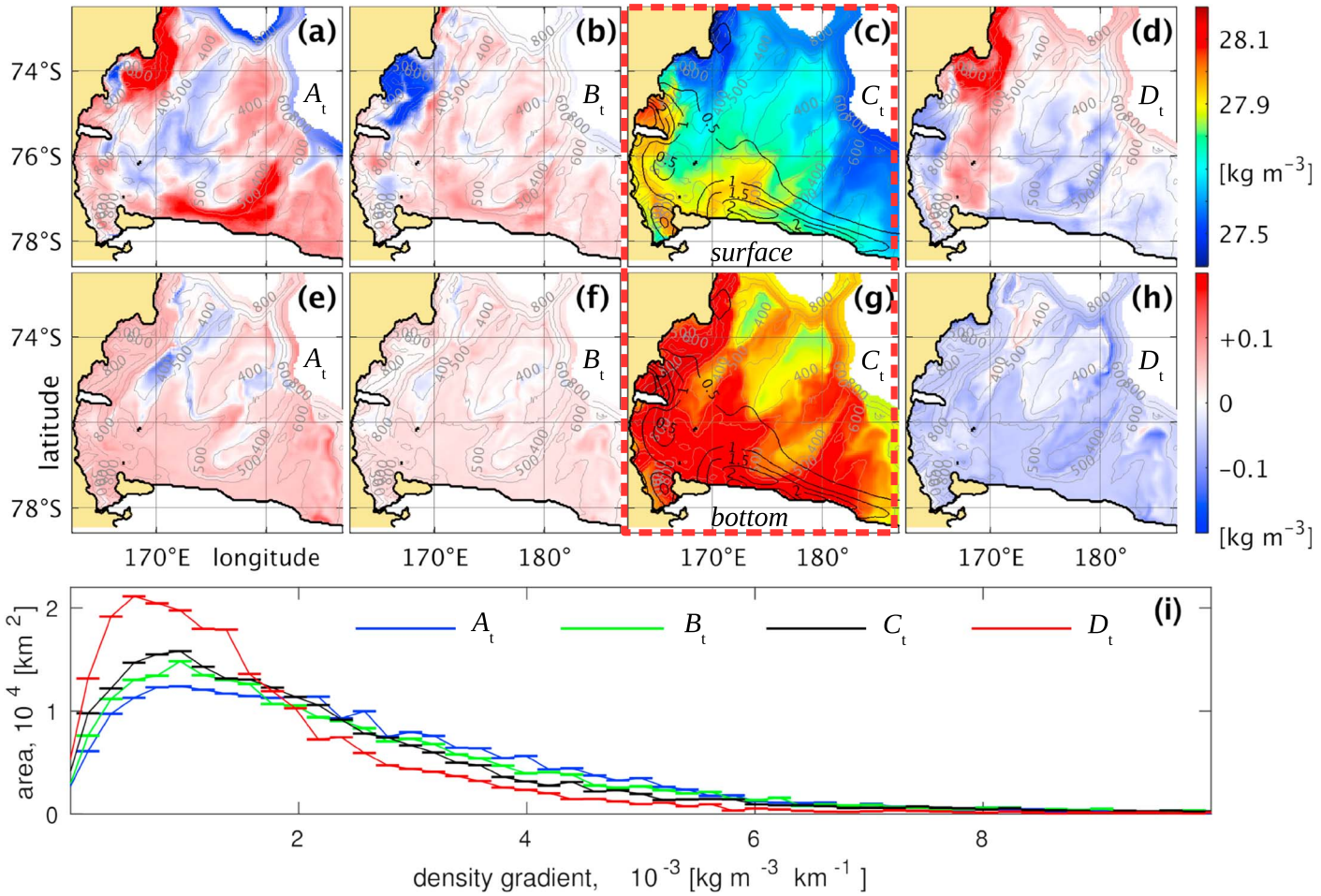

Figure 8. Potential density anomaly over the continental shelf in May for the four different wind stress cases (with tides). Gray contours are model bathymetry. (c) and (g) Density anomaly in the C_t case of the surface and bottom sigma layer, respectively (top colorbar); solid black contours show sea ice production in May in [m/year]. (a), (b), and (d) Differences to (c), comparing surface density of the other tidal cases to C_t; (e), (f), and(h) Differences to (g) in bottom density (bottom colorbar). (i) Distribution of lateral surface density gradients in the western Ross Sea from 160°E–180°; bin size 2×10^{-4} kg·m^{-3}·km^{-1}.

0.2 Sv in May, but low compared to plumes of 0.4 Sv measured in November 2007 (Robinson et al., 2014). The 2007/2008 summer had unusually high sea ice concentration, in particular fast ice in McMurdo Sound due to the large icebergs residing in the south-western Ross Sea 2000–2005 (Brunt et al., 2006; Robinson & Williams, 2012). Conditions were very different from the RSSM's climatological forcing.

While Robinson et al. (2014) conclude their plumes originate under the RIS, results of the nondissipative tracer experiment suggests that more than 90% (comparison of tracer budgets) of the northward flowing fresh water component in McMurdo Sound is melt from the MMIS base. However, due to the geometrical limitations of the sigma-coordinate system in realistically representing the transition between floating the ice shelf and the grounded ice sheet, melting at the grounding line is possibly underestimated by the RSSM. Furthermore, results not presented here agree with Stern et al. (2013) in suggesting that most of the heat responsible for the strong MMIS melting is summer surface-warmed water advected from the RSP region. Summer heat fluxes are possibly overprescribed in the RSSM. The combination with comparably short distances between heat source, melt region, and ISW outflow location and thus short process time scales may explain both the domination of MMIS melt in McMurdo Sound and the missing cold water signature associated with the melt water.

In Little America Basin the tracer experiment (Figure 7k) and the oceanographic analysis show significant melt water outflows of 0.2 Sv with small seasonal variation, and at great depth. To the best of our knowledge, there are no observations to confirm this result.

4. Results and Discussion: Sensitivity Experiments

In total, 8 simulations were performed across four different wind stress dissipation and deviation schemes, applied as monthly boundary conditions (Figure 2), each with and without tides. The differences between the wind stress schemes are strongest especially over the western continental shelf and the shelf break. Unlike Smith et al. (2014) and Dinniman et al. (2012) who included wind-driven thermodynamical processes (cooling, sea ice production) at the surface, here we attempt to isolate the mechanical effects of wind stress only, that is, mixing and momentum transfer. Similar experiments are mentioned in Dinniman et al. (2012) but results are not explicitly presented.

4.1. Wind Affected Circulation

In all cases the general circulation patterns, C1–5, and the ASC (labeled in Figure 3b) remain consistent. For the nonzero wind stress tidal cases ASC mean transports in the open ocean (away from coasts) vary between 10–14 Sv (ASC-E/C/W for B_t, C_t, D_t in Table 2). All three cases simulate the ASC along the eastern continental shelf (ASC-E) as stronger by ~1.5 Sv than in the center (ASC-C). The seasonal variability range of 6–8 Sv is similar between ASC-E and ASC-C, but greater compared to 3–5 Sv in the west (only ASC-W shown in Figure 3e). The zero wind stress case (A_t) shows significantly lower mean ASC transport of 3–7 Sv (ASC-E/C/W, Table 2), but maintains the temporal variability pattern of the other cases and a very similar variability range of 3 Sv (ASC-W, Figure 3e).

Previous modeling efforts (Mathiot et al., 2011) suggested wind forcing as the dominant control mechanism of the ASC. Our results indicate that less than 50% of the ASC transport is attributed to direct transfer of atmospheric momentum. No evidence can be found linking atmospheric control to the large seasonal variability of ASC transport in the Ross Sea that appears on similar magnitudes and timing in all wind stress cases (Figure 3e). Other model studies yield similar conclusions and emphasize the importance of density gradients driving the deep Ross Sea circulation (Z. Wang & Meredith, 2008). Nevertheless, much of the model's baroclinicity in the slope front is imposed by the World Ocean Atlas 2009 boundary conditions. As the isopycnal structure along the slope front was to some extent likely forced by winds, a circumpolar model would be more suitable to investigate further aspects of the ASC's wind dependency.

Over the continental shelf we find the strength of the circulation weakens, apart from cavity outflow in C4, with increasing wind stress (Table 2). Moreover, the on-flow of mCDW with subsequent heat transport decreases with stronger winds. This partly confirms results by Smith et al. (2014). We argue that the circulation over the Ross Sea continental shelf is predominantly geostrophic, driven by lateral density gradients induced through sea ice production, in particular in the polynyas. This supports Q. Wang et al. (2013) who attribute exchange flows near the shelf break to the intensification of CDW-HSSW gradients. First, we explain the slowing circulation for higher wind stresses by increased mixing near the surface which leads to the production of less dense water in the model (Figure 8). Simulation D_t (strongest winds; same parameterized sea ice production) produces the least HSSW (as defined in this study $\sigma > 28$ kg/m^3) in the RSP, thus weakening the gravity-driven circulation in C4, under the RIS (Table 2, Ross Island Current). Second, stronger wind stresses smear out the density gradients horizontally. This is illustrated by weaker density gradient distribution for the strongest wind model D_t (Figure 8i).

The net northward HSSW export via the Drygalski Basin and Trough of 0.44 Sv in the D_t case (0.46 Sv in the A_t case, Table 2) indicates that HSSW production volumes generated in the TNBP are less wind affected. Although bottom density in Drygalski Basin decreases by <0.1 between C_t and D_t, similar to the RSP region (Figures 8g and 8h), the more active TNBP (higher salt flux concentrations) maintains a sufficiently high density to be well above the HSSW threshold in this study.

It is not clear why the northward flow under the central RIS (C4), presumably forced by buoyancy generated through melting under the central southern cavity, shows similar transport of ~1 Sv in the cases A_t, B_t, C_t, and weakens only in the D_t case (−20%). Cavity heat inflow decreases by 40% from A_t to B_t and by 30% from C_t to D_t (Table 2, past 79°S). Thermal energy from the open ocean represents the first component in the relay chain of physical processes driving the thermohaline overturning circulation: heat import, heat diffusion toward the ice-ocean interface, melting, and conversion of fresh water buoyancy to kinetic energy via a sloping ice shelf base. Its decrease would be expected to have a greater effect on the outflow. We speculate that an additional geostrophic baroclinic component arising between the well-ventilated western RIS cavity and the quieter eastern part contributes to the forcing of the northward flow band of C4 under the central RIS.

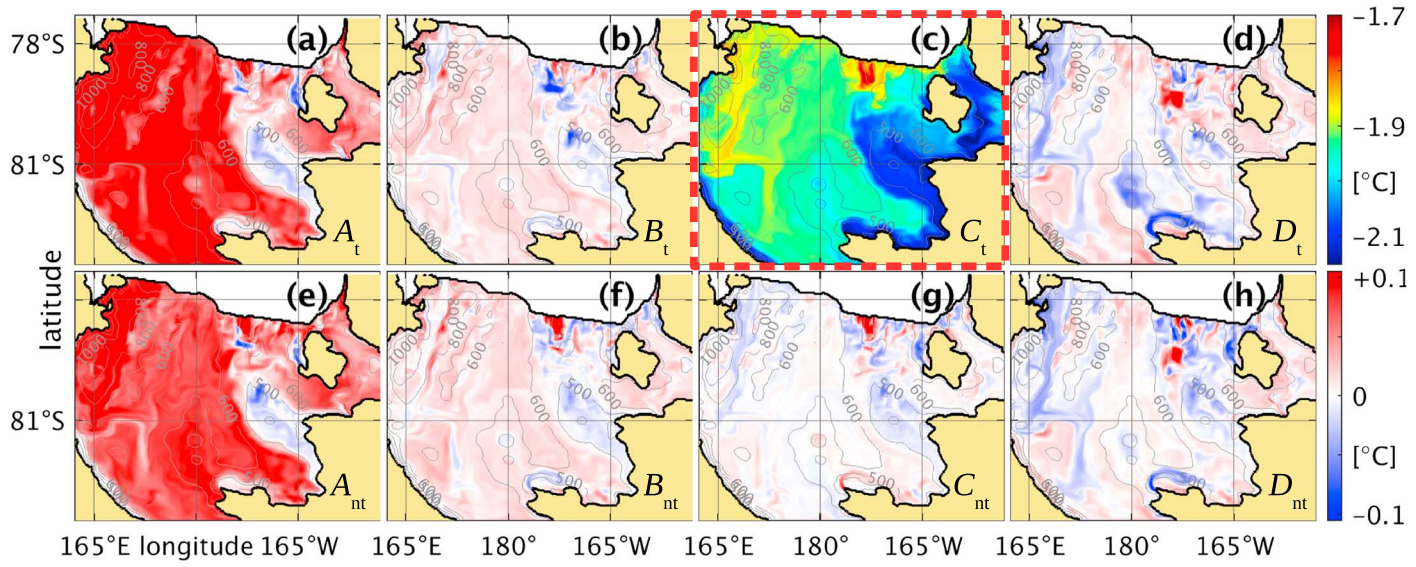

Figure 9. Depth-averaged potential temperature in the RIS cavity for eight different simulation cases. Contours are bathymetry. (a), (b), and (d)–(h) are differences from (c), which shows the temperature for the most realistic simulation case C_t. Colorbars are potential temperature (top, for (c)) and temperature difference (bottom, for (a), (b), (d)–(h)).

4.2. Basal Melting

Overall oceanic heat transport into the interior of the continental shelf (southward of transect 3 in Figure 4a) reduces by 3.6 TW between the zero and the strongest wind stress case when tides are included (A_t, D_t, respectively in Table 2). The 0.29 TW less thermal energy enters the remote cavity (southward of 79°S, transect 3 in Figure 7g). Two factors contribute a weaker winter circulation underneath the RIS (transport in Table 2) and colder water temperatures, by ∼0.1° C (Figures 9a–9d, Table 2) in the D_t case. Consequently, stronger wind stresses result in a colder cavity. The net melt rate decreases by 6.2 cm/year (A_t 13.5 cm/year, D_t 7.3 cm/year; Table 2).

Under the central-eastern RIS, south of the intrusion region over Hayes Bank, the opposite behavior is detected. The strongest wind stress case is 0.2° C warmer than the zero case (Figures 9a and 9d), which is counter intuitive as less mCDW is advected toward the ice shelf in that region (Hayes Bank in Table 2). Analysis not presented in this study suggests that the vorticity-related processes allowing mCDW to penetrate past the barotropic barrier imposed by the RIS edge are largely independent of mCDW resupply from the shelf break. Instead, wind-driven dynamics near the RIS edge may play a role in these processes.

4.3. Tidal Sensitivity

Cavity temperatures are very similar between corresponding tidal and nontidal simulations, except for the region over the southern extent of Hayes Bank (Figure 9). This is attributed to the role of tidal interaction with the RIS edge in the aforementioned vorticity-related mechanism that allows mCDW access to the cavity. The bimodal change pattern in average temperature over Hayes Bank is comparable to the spatial distribution of melt rate differences between tidal and nontidal simulations in Arzeno et al., 2014. However, tidally induced melt differences in the RSSM are low, on the order of 1%, which is not comparable to results from similar studies for the RIS and other big ice shelves (+25–30%, RIS, Arzeno et al., 2014; +50%, Pine Island Ice Shelf, Robertson, 2013; +25%, Filchner-Ronne Ice Shelf, Makinson et al., 2011). While Mueller et al. (2018) also find small differences in total integrated simulated melt with and without tides for the Filchner-Ronne Ice Shelf, their regional melting and freezing patterns change significantly.

We suspect the RSSM has difficulties in generating the isothermal mixed layer observed under the RIS and other ice shelves (Jacobs et al., 1979). Two components are important in the vertical heat transfer toward the base of the ice shelf: the friction velocity as the control parameter of turbulent exchange and the vertical temperature gradient. In regions of high flow velocities under the RIS our simulations reproduce the isothermal layer sufficiently well, and temperature gradients are comparable to observations. Nevertheless, where flows are very small, outside the main circulation pathways of feature C4, the modeled temperature rises logarithmically with increasing depth, starting at the ice-ocean boundary. In these conditions vertical temper-

ature diffusion dominates. In combination with that the RSSM's melt calculation implicitly retains a minimum boundary salinity at the ice-ocean interface, that possibly leads to unrealistically high melting in nontidal and quiet circulation conditions. When tides are included the additional mixing energy moves the solution for the temperature field closer to reality and the top layer becomes more isothermal in less circulated areas. Heat transport is dominated by tide-generated turbulence which creates a more uniform temperature distribution. However, at the same time heat diffusion driven by temperature gradients largely diminishes. Thus, one physical process of heat transport enhances with tides and compensates for the other that is weakening.

Assessing the spatial patterns of melt rate differences from tides in Arzeno et al. (2014) (their Figure 8c) yields another possible explanation for the lower value of tidally induced melting in the RSSM relative to other studies. Larger melt rate differences in (Arzeno et al., 2014) are concentrated along the front between Hayes Bank and Roosevelt Island and along the McMurdo Ice Shelf and in the the southeast. In the relatively shallow water column under the deep draft of the southeastern RIS the semidiurnal tides show maximum amplitude (Robertson, 2005). Tidally induced velocities there, exceeding 10~cm/s, provide additional energy for vertical heat transport to cause higher mode 1 melting while near the amphidromic points under the western and central RIS (M2, S2; Robertson, 2005) melt rate differences in Arzeno et al. (2014) are low. For reasons of model stability the shallow water column under the deep ice draft in the southeast are not included in the RSSM domain, hence do not contribute to tidally induced melting in our study. The largest melt rate differences in Arzeno et al. (2014) found west of Roosevelt Island and over Hayes Bank correlate with large K1 amplitudes exceeding 40 cm (Robertson, 2005). We speculate that in this region the mixing energy from tides helps bring additional heat sourced from mCDW in contact with the ice shelf base. We argue that in the RSSM without tides the lack of tidally induced vertical heat transfer is compensated by more available mCDW (C_t, C_{nt} in Table 2 and Figures 9c and 9g) thus resulting in very low melt rate differences between tidal and nontidal simulations.

Without doubt the tidally sensitive processes of mCDW penetrating past the barotropic barrier imposed by the ice shelf front and the subduction of surface warmed water needs more investigation (modes 2 and 3 ice shelf melting). Intuitively, the ice draft at the front should play a great role. We speculate that, due to bathymetry smoothing, the ice front depth in Arzeno et al. (2014) is half of that applied in the RSSM, thus allowing greater tidally induced mode 3 and mode 2 heat inflow. The shallower ice shelf front combined with their use of a sea ice model possibly allowing a warmer summer surface layer and applying a different mixing scheme (presumably KPP in (Arzeno et al., 2014), following (Dinniman et al., 2011), Mellor-Yamada in this study) may also explain the higher melting and the higher tidally induced melt rate differences compared to the RSSM.

These comments are speculative and based on assumptions and a brief examination of the vertical ocean structure in the RSSM. A detailed analysis is beyond the scope of this paper.

5. Conclusions

5.1. Circulation Structure and Seasonality

Three anticyclonic (C2, C3, C4) and two cyclonic (C1, C5), persistent circulation features subdivide the dynamic regime over the Ross Sea continental shelf and under the RIS. Mean annual transports are 0.9, 1.0, 1.4, and 1.1 Sv (C1-4, respectively; C5 not quantified), with individual seasonal lows of less than 1 Sv in April.Currents, along the north-south running troughs intensify 2 months after the beginning of the model's polynya sea ice production, starting in April, and reach peaks in August–November, September, and December–January for C1, C2, and C3, respectively. We have presented evidence that the seasonal flow intensification over the continental shelf is predominantly driven by the strengthening of horizontal density gradients through winter sea ice formation; wind appears to play a minor role in their modulation.

5.2. The Currents Under the RIS

Our results confirm a large buoyancy-driven cyclonic circulation feature (C4) that facilitates water exchange in the cavity west of 180°; the eastern cavity is much less ventilated. This has been indirectly suggested by satellite observations which locate most of the RIS basal mass loss under the western side of the shelf (Rignot et al., 2013). The main inflow to the cavity is the strong, narrow Ross Island Current (1.1 Sv average; ~100 km wide). South of Ross Island it merges with a smaller inflow through Haskell Strait to a combined southward current of 1.4 Sv. Both inflow dynamics are fueled by gravity-driven HSSW bottom flows. With the start of sea ice production in the RSP these combined inflows intensify C4 until reaching its annual maximum in November–December. Contributions to this mechanism were also found from HSSW formed in the McMurdo Polynya, which is possibly slightly over prescribed in the SSM/I retrieved boundary conditions. A wider, slower,

and less variable northward flow, centered on the Glomar Challenger Basin, is the main mechanism for the export of water from underneath the RIS.

5.3. TNBP HSSW

Neither the water mass analysis nor the passive tracer experiment yielded any support for the access of TNBP-formed HSSW into the RIS cavity. Its distribution in the south seems confined by the edge of the Drygalski Basin. Instead, most of the HSSW produced in the TNBP drains northward toward the shelf break near Cape Adare. We speculate that changes in the TNBP, from a collapse of the Drygalski Ice Tongue, will have greater effects on the Antarctic Bottom Water formation in the western slope region near Cape Adare than changes in the RSP. A second possible effect could be the diversion of RSP HSSW northward. In the RSSM both polynyas supply a dense bottom water table in the south-western Ross Sea, and under the western RIS. If the TNBP source was shutdown, the 1,000 m deep Drygalski Basin would instead be filled by gravity-driven HSSW flows from the RSP region. This in turn could slow down C4 and contribute to cooling the RIS cavity.

5.4. Wind Stress Sensitivity

Results of the sensitivity study across four different wind stress schemes suggest that an increase in atmospheric forcing causes an overall slow down of the circulation over the continental shelf and in the cavity. We attribute this to wind stress-induced weakening of lateral density gradients associated with controlling the circulation. On-shelf heat transport decreases with less mCDW intrusion onto the shelf which is consistent with Smith et al. (2014). We hypothesize that three possible effects of global warming, a weakening of the HSSW production in the polynyas, a dwindling summer sea ice cover, and an increase in extreme wind events in the Southern Ocean, may result in a cooling of the RIS cavity, slowing the ice shelf's melting. This has been suggested by Dinniman et al. (2012) for deeper ice shelf drafts along the WAP where there might be less melting in scenarios of stronger winds. While at the WAP it is attributed to the removal of heat from deeper waters through mixing, we propose an additional effect of slowing ocean currents.

5.5. Ice Shelf Protection Mechanism

The specific ocean floor topography in combination with the circulation structure presented in this study leads us to speculate that the hypothesis of a cavity that cools with increasing wind stresses holds even with greater and warmer mCDW intrusions onto the continental shelf: (1) both cavity inflow locations, the depression between Franklin Island, Ross Island and Ross Bank, and McMurdo Sound are oceanographically decoupled from the deep Southern Ocean. So mCDW has no direct access to these inflow channels and mCDW presence is topographically confined to the slopes of Crary Bank, Pennell Bank, and Ross Bank (C1-3); (2) the winter deep convection in the RSP and smaller MMSP eliminates any remaining heat signal that may have been advected here; (3) the intensification of gravity-driven southward flows starts *after* the deep convection initiates. Therefore, melt potential is sourced solely from the difference between the freezing temperatures at surface and depth and not from potentially warming Southern Ocean water. This can be viewed as a threefold mechanism for protecting the deep base of the RIS from exposure to oceanic heat. For these reasons, we also confirm the RIS is host to a *cold-cavity* (Joughin et al., 2012). Processes similar to the heat blockage by winter deep convection have been suggested for the Totten Ice Shelf and the Mertz Glacier Tongue (Cougnon et al., 2013; Gwyther et al., 2014) with the difference that the presence of dense HSSW acts to prevent direct flow of mCDW underneath the ice.

5.6. Concluding Comments & Outlook

The sensitivity experiments in this study deliberately applied the same surface thermodynamic exchanges in all simulations. Brine rejection from sea ice production, and thus HSSW formation is decoupled from the wind stress to ensure the salt released by sea ice is kept constant between the simulations. Accounting (in part) for the inconsistency between wind stress and ice formation, the three nonzero wind cases maintain similar wind stresses in the polynyas where sea ice concentration is low and most of the HSSW is generated. Therefore, the experiment of applying different wind stresses has stronger effects over the edge of the polynyas where winter-intensified density gradients are most prominent. This configuration circumnavigates the problem that, in reality, stronger winds may enhance the dense water formation and thus compensate for the effects investigated in this study. Each represents one component in the set of driving mechanisms. The setup in this study allows us to isolate, investigate, and quantify the circulation impacts of wind-induced lateral mixing.

On the other hand, it has been shown that model wind forcing of temporal resolution coarser than daily leads to an underrepresentation of mixing in the surface layer and hence larger surface property gradients (Kamenkovich, 2005; Kara et al., 2005; Lee & Liu, 2005; Sui et al., 2003). Consequently, the weakening of shelf

sea circulation with increasing wind stress may in fact be greater than shown in this study that uses monthly forcing fields. Furthermore, the observed freshening of HSSW in the Ross Sea (Jacobs et al., 2002; Jacobs & Giulivi, 2010) may also contribute to changing circulation, although the origin of the freshening over the past six decades is unclear. If it was from melting glaciers and ice shelves located upstream along the Amundsen Coast, the freshening should be concentrated in the eastern Ross Sea continental shelf (tracer study results not presented here). We speculate this could strengthen the general east to west density gradient in the Ross Sea (isopycnals are tilted upward toward the west) and thus enhance southward flows near the surface and northward flows near the bottom. However, this is highly speculative and there are many other effects the freshening could have on the system such as strengthening in situ sea ice production by increasing freezing temperatures or stabilizing the surface stratification delaying the deep convection from sea ice production. It is also conceivable that if resident water masses are fresher and lighter polynya-produced HSSW will induce greater density gradients and possibly increase the circulation.

Possible climate change effects such as increased summer surface warming, deepening of the summer mixed layer over the shelf, and shorter periods of winter surface cooling were also not included in the simulations. These changes also might compensate the negative feedbacks (cooler cavity) through increased wind stress, reduced density gradients, shrinking sea ice cover, and the ice shelf protection mechanism proposed in section 5.5. Our hypothesis that stronger winds will slow down the winter circulation needs further verification with a coupled sea ice-ocean model and should be tested with different mixing and advection schemes. More data from field observation and lab experiments are required to better quantify the effect of sea ice on the transfer of wind stress to the ocean.

Acknowledgments
Funding for this research was provided by: University of Otago, Departmental Scholarship; NIWA research grant; New Zealand Ministry of Business, Innovation, and Employment (MBIE) research programmes CO1X1226, *Ross Sea Climate and Ecosystem*,and C01X1710, *ROSS RAMP*; NIWA Strategic Science Investment Fund and the Deep South National Science Challenge. Takeshi Tamura kindly provided winter surface flux data for the Ross Sea. GODAS data, NCEP-DOE 2 Reanalysis, and NCEP/NCAR Reanalysis 1 data were provided by the NOAA/OAR/ESRL PSD, Boulder, Colorado, USA, from their Web site at https://www.esrl.noaa.gov/psd/. The authors wish to acknowledge the contribution of the NeSI high-performance computing facilities to this research. New Zealand's national facilities are provided by the NZ eScience Infrastructure and funded jointly by NeSI's collaborator institutions and through the Ministry of Business, Innovation and Employment's Research Infrastructure programme (https://www.nesi.org.nz). Craig Stevens and Graham Rickard contributed very helpful insights to contextualize model results with observation data. We also thank David Gwyther and another, anonymous reviewer for providing invaluable improvements to our manuscript. The Fortran build code, header file and model run time options for the C_t case can be accessed under https://github.com/sj-science/RSSM_ROMS.git.

References

Abernathey, R. P., Cerovecki, I., Holland, P. R., Newsom, E., Mazloff, M., & Talley, L. D. (2016). Water-mass transformation by sea ice in the upper branch of the southern ocean overturning. *Nature Geoscience*, *9*(8), 596–601. https://doi.org/10.1038/ngeo2749

Allen, J. S., Newberger, P. A., & Federiuk, J. (1995). Upwelling circulation on the Oregon continental shelf. Part I: Response to idealized forcing. *Journal of Physical Oceanography*, *25*(8), 1843–1866. https://doi.org/10.1175/1520-0485(1995)025<1843

Antonov, J. I., Seidov, D., Boyer, T. P., Locarnini, R. A., Mishonov, A. V., Garcia, H. E., et al. (2010). World Ocean Atlas 2009, Volume 2: Salinity, U.S. Gov. Print. Off., Washington, DC.

Arzeno, I. B., Beardsley, R. C., Limeburner, R., Owens, B., Padman, L., Springer, S. R., et al. (2014). Ocean variability contributing to basal melt rate near the ice front of Ross Ice Shelf, Antarctica. *Journal of Geophysical Research: Oceans*, *119*, 4214–4233. https://doi.org/10.1002/2014JC009792

Ashford, J., Dinniman, M. S., Brooks, C., Andrews, A. H., Hofmann, E. E., Cailliet, G., et al. (2012). Does large-scale ocean circulation structure life history connectivity in Antarctic toothfish (Dissostichus mawsoni)? *Canadian Journal of Fisheries and Aquatic Sciences*, *69*(12), 1903–1919. https://doi.org/10.1139/f2012-111

Assmann, K. M., Hellmer, H. H., & Beckmann, A. (2003). Seasonal variation in circulation and water mass distribution on the Ross Sea continental shelf. *Antarctic Science*, *15*(1), 3–11. https://doi.org/10.1017/S0954102003001007

Assmann, K. M., & Timmermann, R. (2005). Variability of dense water formation in the Ross Sea. *Ocean Dynamics*, *55*(2), 68–87. https://doi.org/10.1007/s10236-004-0106-7

Barry, J. P., & Dayton, P. K. (1988). Current patterns in McMurdo Sound, Antarctica and their relationship to local biotic communities. *Polar Biology*, *8*(5), 367–376. https://doi.org/10.1007/BF00442028

Behringer, D., & Xue, Y. (2004). Evaluation of the global ocean data assimilation system at NCEP: The Pacific Ocean. In *Eighth Symposium on Integrated Observing and Assimilation Systems for Atmosphere, Oceans, and Land Surface, AMS 84th Annual Meeting* (pp. 11–15). Seattle, Washington: Washington State Convention and Trade Center.

Bergamasco, A., Carniel, S., & Valeri, L. C. (1999). Reconstructing the general circulation of the Ross Sea (Antarctica) using a robust diagnostic model, *Oceanography of the Ross Sea Antarctica* (pp. 119–134). Italy, Milan, Milano: Springer-Verlag Italia. https://doi.org/10.1016/S0924-7963(00)00059-2

Bergamasco, A., Defendi, V., & Meloni, R. (2002). Some dynamics of water outflow from beneath the Ross Ice Shelf during 1995 and 1996. *Antarctic Science*, *14*(1), 74–82. https://doi.org/10.1017/S0954102002000603

Brunt, K. M., Sergienko, O., & MacAyeal, D. R. (2006). Observations of unusual fast-ice conditions in the southwest Ross Sea, Antarctica: Preliminary analysis of iceberg and storminess effects. *Annals of Glaciology*, *44*, 183–187. https://doi.org/10.3189/172756406781811754

Budgell, W. P. (2005). Numerical simulation of ice-ocean variability in the Barents Sea region. *Ocean Dynamics*, *55*(3-4), 370–387. https://doi.org/10.1007/s10236-005-0008-3

Carter, L., McCave, I. N., & Williams, M. J. M. (2008). Circulation and water masses of the Southern Ocean: A review. In *Developments in Earth and Environmental Sciences* (Vol. 8, pp. 85–114): Elsevier BV. https://doi.org/10.1016/S1571-9197(08)00004-9

Castagno, P., Falco, P., Dinniman, M. S., Spezie, G., & Budillon, G. (2016). Temporal variability of the Circumpolar Deep Water inflow onto the Ross Sea continental shelf. *Journal of Marine Systems*, *166*, 37–49. https://doi.org/10.1016/j.jmarsys.2016.05.006

Cole, S. T., Timmermans, M.-L., Toole, J. M., Krishfield, R. A., & Thwaites, F. T. (2014). Ekman veering, internal waves, and turbulence observed under Arctic sea ice. *Journal of Physical Oceanography*, *44*(5), 1306–1328. https://doi.org/10.1175/JPO-D-12-0191.1

Comiso, J. C., Kwok, R., Martin, S., & Gordon, A. L. (2011). Variability and trends in sea ice extent and ice production in the Ross Sea. *Journal of Geophysical Research*, *116*, C04021. https://doi.org/10.1029/2010JC006391

Cougnon, E. A., Galton-Fenzi, B. K., Meijers, A. J., & Legrésy, B. (2013). Modeling interannual dense shelf water export in the region of the Mertz Glacier Tongue (1992–2007). *Journal of Geophysical Research: Oceans*, *118*, 5858–5872. https://doi.org/10.1002/2013JC008790

Davey, F. (2004). *Ross Sea bathymetry, 1:2,000,000, Version 1.0, Institute of Geological & Nuclear Sciences Geophysical Map 16*. Lower Hutt, New Zealand: Institute of Geological & Nuclear Sciences Limited.

Depoorter, M. A., Bamber, J. L., Griggs, J. A., Lenaerts, J. T. M., Ligtenberg, S. R. M., van den Broeke, M. R., & Moholdt, G. (2013). Calving fluxes and basal melt rates of Antarctic ice shelves. *Nature*, *502*(7469), 89–92. https://doi.org/10.1038/nature12567

Dinniman, M. S., Klinck, J. M., & Hofmann, E. E. (2012). Sensitivity of Circumpolar Deep Water transport and ice shelf basal melt along the west Antarctic Peninsula to changes in the winds. *Journal of Climate*, *25*(14), 4799–4816. https://doi.org/10.1175/JCLI-D-11-00307.1

Dinniman, M. S., Klinck, J. M., Smith, J., & Walker, O. (2003). Cross-shelf exchange in a model of the Ross Sea circulation and biogeochemistry. *Deep-Sea Research Part II: Topical Studies in Oceanography*, *50*(22-26), 3103–3120. https://doi.org/10.1016/j.dsr2.2003.07.011

Dinniman, M. S., Klinck, J. M., Smith, J., & Walker, O. (2007). Influence of sea ice cover and icebergs on circulation and water mass formation in a numerical circulation model of the Ross Sea, Antarctica. *Journal of Geophysical Research*, *112*, C11013. https://doi.org/10.1029/2006JC004036

Dinniman, M. S., Klinck, J. M., Smith, J., & Walker, O. (2011). A model study of Circumpolar Deep Water on the West Antarctic Peninsula and Ross Sea continental shelves. *Deep-Sea Research Part II: Topical Studies in Oceanography*, *58*(13-16), 1508–1523. https://doi.org/10.1016/j.dsr2.2010.11.013

Dupont, T. K. (2005). Assessment of the importance of ice-shelf buttressing to ice-sheet flow. *Geophysical Research Letters*, *32*, L04503. https://doi.org/10.1029/2004GL022024

Egbert, G. D., & Erofeeva, S. Y. (2002). Efficient inverse modeling of barotropic ocean tides. *Journal of Atmospheric and Oceanic Technology*, *19*(2), 183–204. https://doi.org/10.1175/1520-0426(2002)019<0183

Feltham, D. L. (2002). The influence of ocean flow on newly forming sea ice. *Journal of Geophysical Research*, *107*(C2), 3009. https://doi.org/10.1029/2000JC000559

Fer, I., McPhee, M. G., & Sirevaag, A. (2004). Conditional statistics of the Reynolds stress in the under-ice boundary layer. *Geophysical Research Letters*, *31*, L15311. https://doi.org/10.1029/2004GL020475

Fer, I., & Sundfjord, A. (2007). Observations of upper ocean boundary layer dynamics in the marginal ice zone. *Journal of Geophysical Research*, *112*, C04012. https://doi.org/10.1029/2005JC003428

Galperin, B., Kantha, L. H., Hassid, S., & Rosati, A. (1988). A quasi-equilibrium turbulent energy model for geophysical flows. *Journal of the Atmospheric Science*, *45*(1), 55–62. https://doi.org/10.1175/1520-0469(1988)045<0055

Galton-Fenzi, B. K., Hunter, J. R., Coleman, R., Marsland, S. J., & Warner, R. C. (2012). Modeling the basal melting and marine ice accretion of the Amery Ice Shelf. *Journal of Geophysical Research*, *117*, C09031. https://doi.org/10.1029/2012JC008214

Goosse, H., & Fichefet, T. (1999). Importance of ice-ocean interactions for the global ocean circulation: A model study. *Journal of Geophysical Research*, *104*(C10), 23,337–23,355. https://doi.org/10.1029/1999JC900215

Gordon, A. L., Orsi, A. H., Muench, R. D., Huber, B. A., Zambianchi, E., & Visbeck, M. (2009). Western Ross Sea continental slope gravity currents. *Deep-Sea Research Part II: Topical Studies in Oceanography*, *56*(13-14), 796–817. https://doi.org/10.1016/j.dsr2.2008.10.037

Gordon, A. L., Zambianchi, E., Orsi, A., Visbeck, M., Giulivi, C. F., Whitworth, T., & Spezie, G. (2004). Energetic plumes over the western Ross Sea continental slope. *Geophysical Research Letters*, *31*, L21302. https://doi.org/10.1029/2004GL020785

Gwyther, D. E., Cougnon, E. A., Galton-Fenzi, B. K., Roberts, J. L., Hunter, J. R., & Dinniman, M. S. (2016). Modelling the response of ice shelf basal melting to different ocean cavity environmental regimes. *Annals of Glaciology*, *57*(73), 131–141. https://doi.org/10.1017/aog.2016.31

Gwyther, D. E., Galton-Fenzi, B. K., Hunter, J. R., & Roberts, J. L. (2014). Simulated melt rates for the Totten and Dalton ice shelves. *Ocean Science*, *10*(3), 267–279. https://doi.org/10.5194/os-10-267-2014

Hallberg, R. (2013). Using a resolution function to regulate parameterizations of oceanic mesoscale eddy effects. *Ocean Modelling*, *72*, 92–103. https://doi.org/10.1016/j.ocemod.2013.08.007

Hattermann, T., Smedsrud, L. H., Nøst, O. A., Lilly, J. M., & Galton-Fenzi, B. K. (2014). Eddy-resolving simulations of the Fimbul Ice Shelf cavity circulation: Basal melting and exchange with open ocean. *Ocean Modelling*, *82*, 28–44. https://doi.org/10.1016/j.ocemod.2014.07.004

Hellmer, H. H. (2004). Impact of Antarctic ice shelf basal melting on sea ice and deep ocean properties. *Geophysical Research Letters*, *31*, L10307. https://doi.org/10.1029/2004GL019506

Hellmer, H. H., & Olbers, D. J. (1989). A two-dimensional model for the thermohaline circulation under an ice shelf. *Antarctic Science*, *1*(4), 325–336. https://doi.org/10.1017/S0954102089000490

Holland, D. M., Jacobs, S. S., & Jenkins, A. (2003). Modelling the ocean circulation beneath the Ross Ice Shelf. *Antarctic Science*, *15*(1), 13–23. https://doi.org/10.1017/S0954102003001019

Holland, D. M., & Jenkins, A. (1999). Modeling thermodynamic ice ocean interactions at the base of an ice shelf. *Journal of Physical Oceanography*, *29*(8), 1787–1800. https://doi.org/10.1175/1520-0485(1999)029<1787:MTIOIA>2.0.CO;2

Hollands, T., Haid, V., Dierking, W., Timmermann, R., & Ebner, L. (2013). Sea ice motion and open water area at the Ronne Polynia, Antarctica: Synthetic aperture radar observations versus model results. *Journal of Geophysical Research: Oceans*, *118*, 1940–1954. https://doi.org/10.1002/jgrc.20158

Hughes, K. G., Langhorne, P. J., Leonard, G. H., & Stevens, C. L. (2014). Extension of an Ice Shelf Water plume model beneath sea ice with application in McMurdo Sound, Antarctica. *Journal of Geophysical Research: Oceans*, *119*, 8662–8687. https://doi.org/10.1002/2013JC009411

Jacobs, S. S. (1991). On the nature and significance of the Antarctic Slope Front. *Marine Chemistry*, *35*(1-4), 9–24. https://doi.org/10.1016/S0304-4203(09)90005-6

Jacobs, S. S., & Giulivi, C. F. (1999). Thermohaline data and ocean circulation on the Ross Sea continental shelf. In *Oceanography of the Ross Sea Antarctica* (pp. 3–16). Milano: Springer.

Jacobs, S. S., & Giulivi, C. F. (2010). Large multidecadal salinity trends near the Pacific–Antarctic continental margin. *Journal of Climate*, *23*(17), 4508–4524. https://doi.org/10.1175/2010JCLI3284.1

Jacobs, S. S., Giulivi, C. F., & Mele, P. A. (2002). Freshening of the Ross Sea during the late 20th century. *Science*, *297*(5580), 386–389. https://doi.org/10.1126/science.1069574

Jacobs, S. S., Gordon, A. L., & Ardai, J. Jr. (1979). Circulation and melting beneath the Ross Ice Shelf. *Science*, *203*(4379), 439–443. https://doi.org/10.1126/science.203.4379.439

Jacobs, S. S., Hellmer, H. H., Doake, C. S. M., Jenkins, A., & Frolich, R. M. (1992). Melting of ice shelves and the mass balance of Antarctica. *Journal of Glaciology*, *38*(130), 375–387. https://doi.org/10.1038/228047a0

Jacobs, S. S., Jenkins, A., Giulivi, C. F., & Dutrieux, P. (2011). Stronger ocean circulation and increased melting under Pine Island Glacier ice shelf. *Nature Geoscience*, *4*(8), 519–523. https://doi.org/10.1038/ngeo1188

Jacobs, S. S., & Weiss, R. F. (1998). Ocean, ice, and atmosphere: Interactions at the Antarctic continental margin. In S. S. Jacobs & R. F. Weiss (Eds.), *Ocean, Ice, and Atmosphere: Interactions at the Antarctic Continental Margin, Antarctic Research Series* (Vol. 75, pp. 380). Washington, DC: American Geophysical Union. https://doi.org/10.1029/AR075

Jenkins, A. (1991). Gravity currents beneath ice shelves. In *Glaciers-Ocean-Atmosphere Interactions* (Vol. 208, pp. 177–182). Wallingford: IAHS Publications.

Jenkins, A., Hellmer, H. H., Holland, D. M., Jenkins, A., Hellmer, H. H., & Holland, D. M. (2001). The role of meltwater advection in the formulation of conservative boundary conditions at an ice–ocean interface. *Journal of Physical Oceanography*, *31*(1), 285–296. https://doi.org/10.1175/1520-0485(2001)031<0285

Joughin, I., & Alley, R. B. (2011). Stability of the West Antarctic ice sheet in a warming world. *Nature Geoscience*, *4*(8), 506–513. https://doi.org/10.1038/ngeo1194

Joughin, I., Alley, R. B., & Holland, D. M. (2012). Ice-sheet response to oceanic forcing. *Science*, *338*(6111), 1172–6. https://doi.org/10.1126/science.1226481

Kaleschke, L., Lüpkes, C., Vihma, T., Haarpaintner, J., Bochert, A., Hartmann, J., & Heygster, G. (2001). SSM/I sea ice remote sensing for mesoscale ocean-atmosphere interaction analysis. *Canadian Journal of Remote Sensing*, *27*(5), 526–537. https://doi.org/10.1080/07038992.2001.10854892

Kalnay, E., Kanamitsu, M., Kistler, R., Collins, W., Deaven, D., Gandin, L., et al. (1996). The NCEP/NCAR 40-year reanalysis project. *Bulletin of the American Meteorological Society*, *77*(3), 437–471. https://doi.org/10.1175/1520-0477(1996)077<0437

Kamenkovich, I. V. (2005). Role of daily surface forcing in setting the temperature and mixed layer structure of the Southern Ocean. *Journal of Geophysical Research*, *110*, C07006. https://doi.org/10.1029/2004JC002610

Kanamitsu, M., Ebisuzaki, W., Woollen, J., Yang, S.-K., Hnilo, J. J., Fiorino, M., et al. (2002). NCEP-DOE AMIP-II reanalysis (R-2). *Bulletin of the American Meteorological Society*, *83*(11), 1631–1643. https://doi.org/10.1175/BAMS-83-11-1631

Kara, A. B., Hurlburt, H. E., Wallcraft, A. J., & Bourassa, M. A. (2005). Black sea mixed layer sensitivity to various wind and thermal forcing products on climatological time scales. *Journal of Climate*, *18*(24), 5266–5293. https://doi.org/10.1175/JCLI3573R2.1

Kern, S., Kaleschke, L., & Spreen, G. (2010). Climatology of the Nordic (Irminger, Greenland, Barents, Kara and White/Pechora) Seas ice cover based on 85 GHz satellite microwave radiometry: 1992–2008. *Tellus A*, *62*(4), 411–434. https://doi.org/10.1111/j.1600-0870.2010.00457.x

Klinck, J. M., & Dinniman, M. S. (2010). Exchange across the shelf break at high southern latitudes. *Ocean Science*, *6*(2), 513–524. https://doi.org/10.5194/os-6-513-2010

Kohut, J., Hunter, E., & Huber, B. (2013). Small-scale variability of the cross-shelf flow over the outer shelf of the Ross Sea. *Journal of Geophysical Research: Oceans*, *118*, 1863–1876. https://doi.org/10.1002/jgrc.20090

Kusahara, K., Hasumi, H., & Williams, G. D. (2011). Impact of the Mertz Glacier Tongue calving on dense water formation and export. *Nature Communications*, *2*(1), 159. https://doi.org/10.1038/ncomms1156

Lazeroms, W. M., Jenkins, A., Hilmar Gudmundsson, G., & Van De Wal, R. S. (2018). Modelling present-day basal melt rates for Antarctic ice shelves using a parametrization of buoyant meltwater plumes. *Cryosphere*, *12*(1), 49–70. https://doi.org/10.5194/tc-12-49-2018

Lee, T., & Liu, W. T. (2005). Effects of high-frequency wind sampling on simulated mixed layer depth and upper ocean temperature. *Journal of Geophysical Research*, *110*, C05002. https://doi.org/10.1029/2004JC002746

Lenn, Y.-D., Rippeth, T. P., Old, C. P., Bacon, S., Polyakov, I., Ivanov, V., & Hölemann, J. (2011). Intermittent intense turbulent mixing under ice in the Laptev Sea continental shelf. *Journal of Physical Oceanography*, *41*(3), 531–547. https://doi.org/10.1175/2010JPO4425.1

Leppäranta, M. (2011). *The Drift of Sea Ice* (pp. 341). Berlin Heidelberg: Springer Science & Business Media.

Lewis, E. L., & Perkin, R. G. (1985). The winter oceanography of McMurdo Sound, Antarctica, oceanology of the antarctic continental shelf. *Antarctic Research Series*, *43*, 145–165.

Liu, Y., Moore, J. C., Cheng, X., Gladstone, R. M., Bassis, J. N., Liu, H., et al. (2015). Ocean-driven thinning enhances iceberg calving and retreat of Antarctic ice shelves. *Proceedings of the National Academy of Sciences*, *112*(11), 3263–3268. https://doi.org/10.1073/pnas.1415137112

Locarnini, R. A., Mishonov, A. V., Antonov, J. I., Boyer, T. P., Garcia, H. E., Baranova, O. K., et al. (2010). World ocean atlas 2009 volume 1: Temperature. U.S. Gov. Print. Off., Washington, DC.

Lüpkes, C., & Birnbaum, G. (2005). Surface drag in the Arctic marginal sea-ice zone: A comparison of different parameterisation concepts. *Boundary-Layer Meteorology*, *117*(2), 179–211. https://doi.org/10.1007/s10546-005-1445-8

MacAyeal, D. R. (1984). Thermohaline circulation below the Ross Ice Shelf: A consequence of tidally induced vertical mixing and basal melting. *Journal of Geophysical Research*, *89*(C1), 597–606. https://doi.org/10.1029/JC089iC01p00597

Mahoney, A. R., Gough, A. J., Langhorne, P. J., Robinson, N. J., Stevens, C. L., Williams, M. J. M., & Haskell, T. G. (2011). The seasonal appearance of ice shelf water in coastal Antarctica and its effect on sea ice growth. *Journal of Geophysical Research*, *116*, C11032. https://doi.org/10.1029/2011JC007060

Makinson, K., Holland, P. R., Jenkins, A., Nicholls, K. W., & Holland, D. M. (2011). Influence of tides on melting and freezing beneath Filchner-Ronne Ice Shelf, Antarctica. *Geophysical Research Letters*, *38*, L06601. https://doi.org/10.1029/2010GL046462

Margolin, L. E. N., & Smolarkiewicz, P. K. (1998). Antidiffusive velocities for multipass donor cell advection. *SIAM Journal on Scientific Computing*, *20*(3), 907–929. https://doi.org/10.1137/S106482759324700X

Marshall, G. J. (2003). Trends in the Southern Annular Mode from observations and reanalyses. *Journal of Climate*, *16*(24), 4134–4143. https://doi.org/10.1175/1520-0442(2003)016<4134

Mathiot, P., Goosse, H., Fichefet, T., Barnier, B., & Gallée, H. (2011). Modelling the seasonal variability of the Antarctic Slope Current. *Ocean Science*, *7*(4), 455–470. https://doi.org/10.5194/os-7-455-2011

McPhee, M. G. (1980). An analysis of pack ice drift in summer. In *Proceedings of the Arctic Ice Dynamics Joint Experiment International Commission on Snow and Ice Symposium* (pp. 62–75). Seattle: University of Washington Press.

McPhee, M. G. (1992). Turbulent heat flux in the upper ocean under sea ice. *Journal of Geophysical Research*, *97*(C4), 5365–5379. https://doi.org/10.1029/92JC00239

McPhee, M. G. (2002). Turbulent stress at the ice/ocean interface and bottom surface hydraulic roughness during the SHEBA drift. *Journal of Geophysical Research*, *107*(C10), 8037. https://doi.org/10.1029/2000JC000633

McPhee, M. G. (2008). Physics of early summer ice/ocean exchanges in the western Weddell Sea during ISPOL. *Deep-Sea Research Part II: Topical Studies in Oceanography*, *55*(8-9), 1075–1097. https://doi.org/10.1016/j.dsr2.2007.12.022

McPhee, M. G., & Martinson, D. G. (1994). Turbulent mixing under drifting pack ice in the Weddell Sea. *Science*, *263*(5144), 218–221. https://doi.org/10.1126/science.263.5144.218

McPhee, M. G., Maykut, G. A., & Morison, J. H. (1987). Dynamics and thermodynamics of the ice/upper ocean system in the marginal ice zone of the Greenland Sea. *Journal of Geophysical Research*, *92*(C7), 7017–7031. https://doi.org/10.1029/JC092iC07p07017

Mellor, G. L., & Yamada, T. (1982). Development of a turbulence closure model for geophysical fluid problems. *Reviews of Geophysics and Space Physics*, *20*(4), 851–875. https://doi.org/10.1029/RG020i004p00851

Mensa, J. A., & Timmermans, M. L. (2017). Characterizing the seasonal cycle of upper-ocean flows under multi-year sea ice. *Ocean Modelling*, *113*, 115–130. https://doi.org/10.1016/j.ocemod.2017.03.009

Moholdt, G., Padman, L., & Fricker, H. A. (2014). Basal mass budget of Ross and Filchner-Ronne ice shelves, Antarctica, derived from Lagrangian analysis of ICES at altimetry. *Journal of Geophysical Research: Earth Surface*, *119*, 2361–2380. https://doi.org/10.1002/2014JF003171

Mueller, R. D., Hattermann, T., Howard, S. L., & Padman, L. (2018). Tidal influences on a future evolution of the Filchner-Ronne Ice Shelf cavity in the Weddell Sea, Antarctica. *The Cryosphere*, *12*, 453–476.

Muench, R., Padman, L., Gordon, A., & Orsi, A. (2009). A dense water outflow from the Ross Sea, Antarctica: Mixing and the contribution of tides. *Journal of Marine Systems*, *77*(4), 369–387. https://doi.org/10.1016/j.jmarsys.2008.11.003

Nøst, O. A., Biuw, M., Tverberg, V., Lydersen, C., Hattermann, T., Zhou, Q., et al. (2011). Eddy overturning of the Antarctic Slope Front controls glacial melting in the Eastern Weddell Sea. *Journal of Geophysical Research*, *116*, C11014. https://doi.org/10.1029/2011JC006965

Orsi, A. H., & Wiederwohl, C. L. (2009). A recount of Ross Sea waters. *Deep-Sea Research Part II: Topical Studies in Oceanography*, *56*(13-14), 778–795. https://doi.org/10.1016/j.dsr2.2008.10.033

Padman, L., Howard, S., Orsi, A. H., & Muench, R. D. (2009). Tides of the northwestern Ross Sea and their impact on dense outflows of Antarctic Bottom Water. *Deep-Sea Research Part II: Topical Studies in Oceanography*, *56*(13-14), 818–834. https://doi.org/10.1016/j.dsr2.2008.10.026

Peterson, A. K., Fer, I., McPhee, M. G., & Randelhoff, A. (2017). Turbulent heat and momentum fluxes in the upper ocean under Arctic sea ice. *Journal of Geophysical Research: Oceans*, *122*, 1439–1456. https://doi.org/10.1002/2016JC012283

Petty, A. A., Feltham, D. L., & Holland, P. R. (2013). Impact of atmospheric forcing on Antarctic continental shelf water masses. *Journal of Physical Oceanography*, *43*(5), 920–940. https://doi.org/10.1175/JPO-D-12-0172.1

Petty, A. A., Holland, P. R., & Feltham, D. L. (2014). Sea ice and the ocean mixed layer over the Antarctic shelf seas. *The Cryosphere*, *8*(2), 761–783. https://doi.org/10.5194/tc-8-761-2014

Reddy, T. E., Holland, D. M., & Arrigo, K. R. (2010). Ross ice shelf cavity circulation, residence time, and melting: Results from a model of oceanic chlorofluorocarbons. *Continental Shelf Research*, *30*(7), 733–742. https://doi.org/10.1016/j.csr.2010.01.007

Renfrew, I. A., Moore, G. W. K., Guest, P. S., & Bumke, K. (2002). A Comparison of surface layer and surface turbulent flux observations over the Labrador Sea with ECMWF analyses and NCEP reanalyses. *Journal of Physical Oceanography*, *32*(2), 383–400.

Rignot, E., Casassa, G., Gogineni, P., Krabill, W., Rivera, A., & Thomas, R. (2004). Accelerated ice discharge from the Antarctic Peninsula following the collapse of Larsen B ice shelf. *Geophysical Research Letters*, *31*, L18401. https://doi.org/10.1029/2004GL020697

Rignot, E., Jacobs, S. S., Mouginot, J., & Scheuchl, B. (2013). Ice-shelf melting around Antarctica. *Science*, *341*(6143), 266–70. https://doi.org/10.1126/science.1235798

Robertson, R. (2005). Baroclinic and barotropic tides in the Ross Sea. *Antarctic Science*, *17*(1), 107–120. https://doi.org/10.1017/S0954102005002506

Robertson, R. (2006). Modeling internal tides over Fieberling Guyot: Resolution, parameterization, performance. *Ocean Dynamics*, *56*(5-6), 430–444. https://doi.org/10.1007/s10236-006-0062-5

Robertson, R. (2013). Tidally induced increases in melting of Amundsen Sea ice shelves. *Journal of Geophysical Research: Oceans*, *118*, 3138–3145. https://doi.org/10.1002/jgrc.20236

Robertson, R., Beckmann, A., & Hellmer, H. H. (2003). M2 tidal dynamics in the Ross Sea. *Antarctic Science*, *15*(1), 41–46. https://doi.org/10.1017/S0954102003001044

Robertson, R., Padman, L., & Levine, M. D. (1995). Fine structure, microstructure, and vertical mixing processes in the upper ocean in the western Weddell Sea. *Journal of Geophysical Research*, *100*(95), 18517. https://doi.org/10.1029/95JC01742

Robinson, N. J., & Williams, M. J. M. (2012). Iceberg-induced changes to polynya operation and regional oceanography in the southern Ross Sea, Antarctica, from in situ observations. *Antarctic Science*, *24*(05), 514–526. https://doi.org/10.1017/S0954102012000296

Robinson, N. J., Williams, M. J. M., Barrett, P. J., & Pyne, A. R. (2010). Observations of flow and ice-ocean interaction beneath the McMurdo Ice Shelf, Antarctica. *Journal of Geophysical Research*, *115*, C03025. https://doi.org/10.1029/2008JC005255

Robinson, N. J., Williams, M. J. M., Stevens, C. L., Langhorne, P. J., & Haskell, T. G. (2014). Evolution of a supercooled Ice Shelf Water plume with an actively growing subice platelet matrix. *Journal of Geophysical Research: Oceans*, *119*, 3425–3446. https://doi.org/10.1002/2013JC009399

Shchepetkin, A. F., & McWilliams, J. C. (2005). The regional oceanic modeling system (ROMS): A split-explicit, free-surface, topography-following-coordinate oceanic model. *Ocean Modelling*, *9*(August), 347–404. https://doi.org/10.1016/j.ocemod.2004.08.002

Skyllingstad, E. D., & Denbo, D. W. (2001). Turbulence beneath sea ice and leads: A coupled sea ice/large-eddy simulation study. *Journal of Geophysical Research*, *106*(C2), 2477–2497. https://doi.org/10.1029/1999JC000091

Smethie, W. M., & Jacobs, S. S. (2005). Circulation and melting under the Ross Ice Shelf: Estimates from evolving CFC, salinity and temperature fields in the Ross Sea. *Deep-Sea Research Part I: Oceanographic Research Papers*, *52*(6), 959–978. https://doi.org/10.1016/j.dsr.2004.11.016

Smith, W. O., Dinniman, M. S., Hofmann, E. E., & Klinck, J. M. (2014). The effects of changing winds and temperatures on the oceanography of the Ross Sea in the 21st century. *Geophysical Research Letters*, *41*, 1624–1631. https://doi.org/10.1002/2014GL059311

Smith, I. J., Langhorne, P. J., Frew, R. D., Vennell, R., & Haskell, T. G. (2012). Sea ice growth rates near ice shelves. *Cold Regions Science and Technology*, *83-84*, 57–70. https://doi.org/10.1016/j.coldregions.2012.06.005

Smith, W. O., Sedwick, P. N., Arrigo, K. R., Ainley, D. G., & Orsi, A. H. (2012). The Ross Sea in a sea of change. *Oceanography*, *25*, 90–103.

Smolarkiewicz, P. K. (1984). Positive definite advection transport algorithm with small implicit diffusion. *Journal of Computational Physics*, *362*(2), 325–362. https://doi.org/10.1016/0021-9991(84)90121-9

Smolarkiewicz, P. K., & Clark, T. L. (1986). The multidimensional positive definite advection transport algorithm: Further development and applications. *Journal of Computational Physics*, *67*(2), 396–438. https://doi.org/10.1016/0021-9991(86)90270-6

Spreen, G., Kaleschke, L., & Heygster, G. (2008). Sea ice remote sensing using AMSR-E 89-GHz channels. *Journal of Geophysical Research*, *113*, C02S03. https://doi.org/10.1029/2005JC003384

St-Laurent, P., Klinck, J. M., & Dinniman, M. S. (2013). On the role of coastal troughs in the circulation of warm Circumpolar Deep Water on Antarctic shelves. *Journal of Physical Oceanography*, *43*(1), 51–64. https://doi.org/10.1175/JPO-D-11-0237.1

Stern, A. A., Dinniman, M. S., Zagorodnov, V. S., Tyler, S. W., & Holland, D. M. (2013). Intrusion of warm surface water beneath the McMurdo Ice Shelf, Antarctica. *Journal of Geophysical Research: Oceans*, *118*, 7036–7048. https://doi.org/10.1002/2013JC008842

Stevens, C. L., Robinson, N. J., Williams, M. J. M., & Haskell, T. G. (2009). Observations of turbulence beneath sea ice in southern McMurdo Sound, Antarctica. *Ocean Science*, *5*(4), 435–445. https://doi.org/10.5194/os-5-435-2009

Stevens, C., Sang Lee, W., Fusco, G., Yun, S., Grant, B., Robinson, N., & Yeon Hwang, C. (2017). The influence of the Drygalski Ice Tongue on the local ocean. *Annals of Glaciology*, *58*, 1–9. https://doi.org/10.1017/aog.2017.4

Stewart, A. L., & Thompson, A. F. (2015). Eddy-mediated transport of warm Circumpolar Deep Water across the Antarctic shelf break. *Geophysical Research Letters*, *42*, 432–440. https://doi.org/10.1002/2014GL062281

Sui, C. H., Li, X., Rienecker, M. M., Lau, K. M., Laszlo, I., & Pinker, R. T. (2003). The role of daily surface forcing in the upper ocean over the tropical Pacific: A numerical study. *Journal of Climate*, *16*(4), 756–766. https://doi.org/10.1175/1520-0442(2003)016<0756

Tamura, T., Ohshima, K. I., & Nihashi, S. (2008). Mapping of sea ice production for Antarctic coastal polynyas. *Geophysical Research Letters*, *35*, L07606. https://doi.org/10.1029/2007GL032903

Thoma, M., Jenkins, A., Holland, D. M., & Jacobs, S. S. (2008). Modelling Circumpolar Deep Water intrusions on the Amundsen Sea continental shelf, Antarctica. *Geophysical Research Letters*, *35*, L18602. https://doi.org/10.1029/2008GL034939

Thomas, R., Rignot, E., Casassa, G., Kanagaratnam, P., Acuña, C., Akins, T., et al. (2004). Accelerated sea-level rise from west Antarctica. *Science*, *306*(5694), 255–258. https://doi.org/10.1126/science.1099650

Timmermann, R., & Hellmer, H. H. (2013). Southern Ocean warming and increased ice shelf basal melting in the twenty-first and twenty-second centuries based on coupled ice-ocean finite-element modelling. *Ocean Dynamics*, *63*(9-10), 1011–1026. https://doi.org/10.1007/s10236-013-0642-0

Timmermann, R., Le Brocq, A. M., Deen, T., Domack, E., Dutrieux, P., Galton-Fenzi, B. K., et al. (2010). A consistent dataset of Antarctic ice sheet topography, cavity geometry, and global bathymetry. *Earth System Science Data Discussions*, *3*(2), 231–257. https://doi.org/10.5194/essdd-3-231-2010

Timmermann, R., Wang, Q., & Hellmer, H. H. (2012). Ice-shelf basal melting in a global finite-element sea-ice/ice-shelf/ocean model. *Annals of Glaciology*, *53*(60), 303–314. https://doi.org/10.3189/2012AoG60A156

Tressler, W. L., & Ommundsen, A. M. (1962). Seasonal Oceanographic Studies in McMurdo Sound, Antarctica (Tech. rep). Washington, U.S: United States. Hydrographic Office.

Turner, J., Comiso, J. C., Marshall, G. J., Lachlan-Cope, T. A., Bracegirdle, T., Maksym, T., et al. (2009). Non-annular atmospheric circulation change induced by stratospheric ozone depletion and its role in the recent increase of Antarctic sea ice extent. *Geophysical Research Letters*, *36*, L08502. https://doi.org/10.1029/2009GL037524

Walker, R. T., Dupont, T. K., Parizek, B. R., & Alley, R. B. (2008). Effects of basal-melting distribution on the retreat of ice-shelf grounding lines. *Geophysical Research Letters*, *35*, L17503. https://doi.org/10.1029/2008GL034947

Wang, Q., Danilov, S., Hellmer, H. H., & Schröter, J. (2010). Overflow dynamics and bottom water formation in the western Ross Sea: Influence of tides. *Journal of Geophysical Research*, *115*, C10054. https://doi.org/10.1029/2010JC006189

Wang, Q., Danilov, S., Hellmer, H. H., Sidorenko, D., Schröter, J., & Jung, T. (2013). Enhanced cross-shelf exchange by tides in the western Ross Sea. *Geophysical Research Letters*, *40*, 5735–5739. https://doi.org/10.1002/2013GL058207

Wang, Z., & Meredith, M. P. (2008). Density-driven Southern Hemisphere subpolar gyres in coupled climate models. *Geophysical Research Letters*, *35*, L14608. https://doi.org/10.1029/2008GL034344

Zhang, J., & Hibler, W. D. (1997). On an efficient numerical method for modeling sea ice dynamics. *Journal of Geophysical Research*, *102*(C4), 8691–8702. https://doi.org/10.1029/96JC03744